

TICRA

Electromagnetic properties
and optical analysis
of the ALMA antennas and
Front Ends

Work was performed under
ESO contract:....

Released by: Christoph
Haupt

Author:

Knud Pontoppidan

October, 2007

S-1430-02

TABLE OF CONTENTS

1. Introduction	1
2. Nominal antenna geometry	2
2.1 Nominal antenna geometry including feeds	2
2.2 Influence of support legs	2
2.2.1 Typical strut contributions	2
2.2.2 AEM support leg design	4
2.2.3 Vertex support leg design	9
2.2.3.1 Introduction.	9
2.2.3.2 Some simplifications.	10
2.2.3.3 Shadowing effects.	13
2.2.3.4 Scattering effects.	13
2.2.3.5 Multiple scattering effects.	14
2.2.3.6 Conclusion.	15
2.3 Influence of Goretex membrane	17
2.4 Influence of reflector panels	19
2.4.1 AEM panels	19
2.4.2 Vertex panels	19
2.4.3 Conclusion on panel effects	21
3. Subreflector	22
3.1 Scattering cone	22
3.1.1 A few words about the Physical Optics model	22
3.1.2 Initial analysis of cone effect	24
3.1.3 Scattering cone parameter variation	28
3.2 Subreflector tilt	30
3.3 Subreflector nutation	32
3.4 Rounded subreflector edge	35

3.4.1	Introduction.	35
3.4.2	Method of moments versus PO+PTD.	35
3.4.3	Method of Moments on modified model.	40
3.4.4	Analytical analysis of rounded edge.	44
3.4.4.1	Review of formulas and results.	44
3.4.4.2	Improved formulation, ALMA results.	47
3.4.4.3	Impact on G/T for ALMA results.	48
3.4.5	Conclusion.	53
4.	Set-up of front ends	54
4.1	Band 1	54
4.2	Band 2	56
4.3	Band 3	58
4.3.1	Feed geometry and analysis	58
4.3.2	Lens geometry and analysis	60
4.3.3	Mirror 1 geometry	63
4.3.4	Mirror 2 geometry	64
4.3.5	Cryostat window and filter geometry	64
4.3.6	GRASP analysis results	65
4.3.7	Accurate Analysis of Grooved Lens	68
4.3.8	Band 3 summary	72
4.4	Band 4	73
4.4.1	Feed geometry	73
4.4.2	Mirror 1 geometry	74
4.4.3	Mirror 2 geometry	75
4.4.4	Cryostat window and filter geometry	75
4.4.5	GRASP analysis results	76
4.4.6	Band 4 summary	77
4.5	Band 5	78
4.6	Band 6	81
4.6.1	Feed geometry	81

4.6.2 Mirror 1 geometry	83
4.6.3 Mirror 2 geometry	85
4.6.4 Cryostat window and filter geometry	87
4.6.5 GRASP analysis results	87
4.6.6 Band 6 summary	93
4.7 Band 7	94
4.7.1 Feed geometry	95
4.7.2 Geometry of the mirrors M1 and M1R	95
4.7.3 Geometry of mirror M2	96
4.7.4 Polarisation grid	97
4.7.5 Cryostat window and filter geometry	97
4.7.6 GRASP analysis results	98
4.7.7 Band 7 summary	102
4.8 Band 8	103
4.9 Band 9	105
4.9.1 Feed geometry	105
4.9.2 Geometry of the mirrors M4 and M4'	106
4.9.3 Geometry of mirror M3	107
4.9.4 Polarisation grid	108
4.9.5 Beam splitters	108
4.9.6 Cryostat window and filter geometry	108
4.9.7 GRASP analysis results	110
4.9.8 Band 9 summary	113
4.10 Band 10	114
4.11 Windows and filters	116
5. Detailed calculations	117
5.1 Calculation of front end efficiencies	117
5.1.1 Introduction.	117
5.1.2 Front-efficiency versus system efficiency.	117
5.1.3 Efficiency formulas.	118

5.1.4 Efficiency results.	119
5.1.5 Conclusion.	123
5.2 Calculation of entire optical system beams	123
5.2.1 File name convention	138
5.3 Calculation of aperture efficiency and G/T	141
5.4 Reflector deformations and beam performance	143
5.4.1 Presentation of the geometrical surface deformations	143
5.4.1.1 Deformations for the AEM antenna	143
5.4.1.2 Deformations for the Vertex antenna	149
5.4.2 Overview of RF calculations	154
5.4.3 RF calculations for the AEM antenna	157
5.4.3.1 Surface deformations	157
5.4.3.2 Panel alignment and deformations	163
5.4.4 RF calculations for the Vertex antenna	170
5.4.4.1 Surface deformations	170
5.4.4.2 Panel alignment and deformations	176

5. Detailed calculations

5.1 Calculation of front end efficiencies

5.1.1 *Introduction.*

The aperture efficiency of a reflector antenna (η) is linked to the directivity of the antenna through the equation

$$D = \frac{4\pi A}{\lambda^2} \eta \quad (5.1)$$

where D is the directivity and A is the area of the aperture. An efficiency of unity corresponds to the case, where the aperture illumination is constant in both amplitude and phase. Since many factors contribute to the actual illumination of the aperture, e.g. multiple scattering from the subreflector and the support structure, it is not in general possible to associate the efficiency with the front-end design alone. To do so requires that certain simplifications are introduced. More precisely, in the following the efficiencies of the front-ends will be calculated based on the assumption that they are illuminating an equivalent paraboloid with the equivalent focal length (f_0) of 96000mm, and diameter equal the real main reflector. The front-end is assumed to be placed in the focal point of the equivalent paraboloid. Furthermore we shall consider the gain of the antenna to include the effect of power loss due to spill-over and cross-polarisation. The equation we consider is therefore

$$G_{co} = \frac{4\pi A}{\lambda^2} \eta_{spill-over} \eta_{polarisation} \eta_{amplitude} \eta_{phase}. \quad (5.2)$$

where the efficiency for the co-polar gain (G_{co}) has been divided into explicit values for spill-over loss, polarisation loss, loss due to amplitude variations and loss due to phase variations over the aperture of the equivalent paraboloid.

5.1.2 *Front-efficiency versus system efficiency.*

To understand how the approximations introduced in Section 5.1.1 influence the relationship between the front-end efficiencies and the aperture efficiency of the entire ALMA antenna, a small experiment will be introduced, using 230 GHz as a representative frequency. Consider first the nominal ALMA design, a feed in the external focus illuminating the subreflector through a hole with radius 375mm, and a centre cone on the subreflector to redirect the radiation of the main reflector. The feed is assumed to emit a

Gaussian beam with a 12 dB taper at the edge of the subreflector (3.58°). Ignoring the support structure, the maximum gain is 88.20 dBi. Consider next a geometry where there is no hole in the main reflector (ignoring the problem of blocking) and no centre cone on the subreflector. The maximum gain would be 88.26 dBi. Consider finally the equivalent paraboloid with the same feed at the focus. The maximum gain is 88.32 dBi. The total spill-over in the three cases vary with only 0.01 dB, so the difference in gain must be ascribed to variations in the illumination of the aperture. In particular, the difference between the two latter cases show, that the scattering from the subreflector occurs in a region where the field from the feed still retains Gaussian properties, so a not insignificant phase variation occurs in the aperture, whereas for the equivalent paraboloid the phase in the aperture is almost exactly constant. With this caveat we proceed to define the formulas for each of the four efficiencies of the front-ends.

5.1.3 Efficiency formulas.

The efficiency of the equivalent paraboloid illuminated by a particular front-end is calculated as the ratio of certain integrals over the aperture. Since the subtended angle of the aperture seen from the feed is small, we shall replace the aperture integrals with integrals over the solid angle Ω , defined through

$$\Omega = \int_{\Omega} d\omega = \int_0^{2\pi} \int_0^{\theta_m} \sin \theta d\theta d\phi = 2\pi(1 - \cos(\theta_m)). \quad (5.3)$$

with $\theta_m = 3.58^\circ$. Thus the aperture, A , and the equivalent focal length, f_0 , are connected through the approximate formula: $A = f_0^2 \Omega$. The effects on the efficiencies of transmission losses in filters and windows cannot be included exactly, but estimates are given in Section 4.11.

We shall calculate the following four integrals:

- 1) I_1 : integral of total power over Ω
- 2) I_2 : integral of co-polar power over Ω
- 3) I_3 : integral of co-polar amplitude over Ω
- 4) I_4 : absolute value of integral of co-polar (complex) field over Ω , where it is assumed that all fields are normalized such that the total power emitted by the feed is 4π .

$$I_1 = \int_{\Omega} |\mathbf{E}_{tot}|^2 d\omega. \quad (5.4)$$

$$I_2 = \int_{\Omega} |\mathbf{E}_{co}|^2 d\omega. \quad (5.5)$$

$$I_3 = \int_{\Omega} |\mathbf{E}_{co}| d\omega. \quad (5.6)$$

$$I_4 = \left| \int_{\Omega} \mathbf{E}_{co} d\omega \right|. \quad (5.7)$$

The four efficiencies introduced in (5.2) are now defined through:

$$\eta_{spill-over} = \frac{I_1}{4\pi}. \quad (5.8)$$

$$\eta_{polarisation} = \frac{I_2}{I_1}. \quad (5.9)$$

$$\eta_{amplitude} = \frac{I_3^2}{\Omega I_2}. \quad (5.10)$$

$$\eta_{phase} = \frac{I_4^2}{I_3^2}. \quad (5.11)$$

G_{co} in (5.2) then becomes

$$G_{co} = \frac{f_0^2}{\lambda^2} I_4^2. \quad (5.12)$$

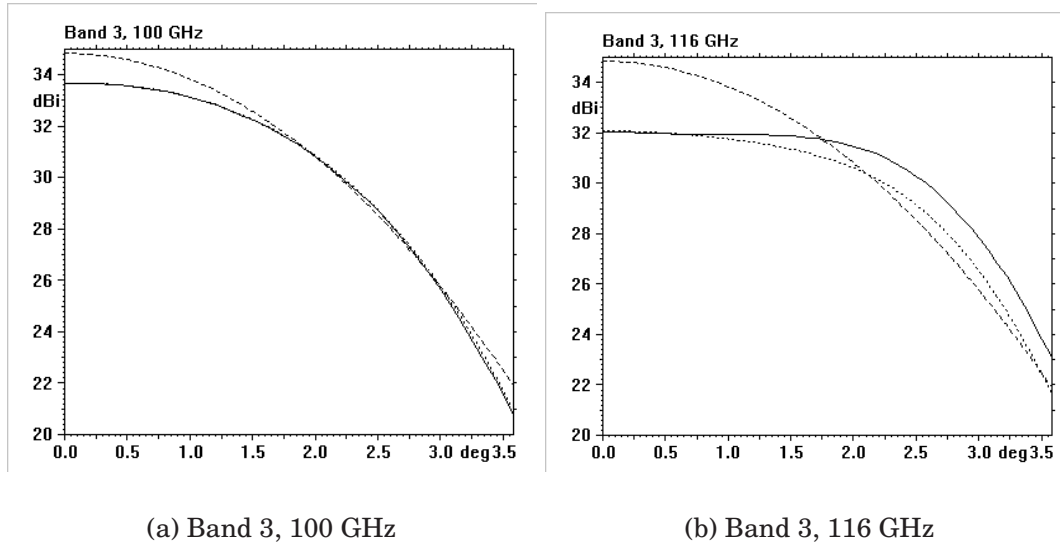
When data from the example in Section 5.1.2 are entered, the gain calculated is within 0.01 dB of the result for the equivalent paraboloid.

5.1.4 Efficiency results.

The formulas from Section 5.1.3 will now be used to calculate the efficiencies of the front-ends, for which data are available, at the centre frequency of the relevant band, and the results will be compared to efficiencies of an exact Gaussian beam feed at the same frequency. The data for the Gaussian feeds are listed in Table 5.1.

<i>Band</i>	Phase front radius [mm]	Beam radius [mm]
Band 1, 31.3 GHz	-21275.52166	57.32333442
Band 2, 78 GHz	-0.1207552e14	22.29008727
Band 3, 100 GHz	∞	18.61469643
Band 3, 116 GHz	∞	16.05453645
Band 4, 144 GHz	∞	12.45339595
Band 5, 187 GHz	∞	9.598899539
Band 6, 243 GHz	∞	7.4490
Band 7, 324 GHz	-69030708.46	5.588136287
Band 8, 442 GHz	∞	4.094947923
Band 9, 661 GHz	∞	2.728968572

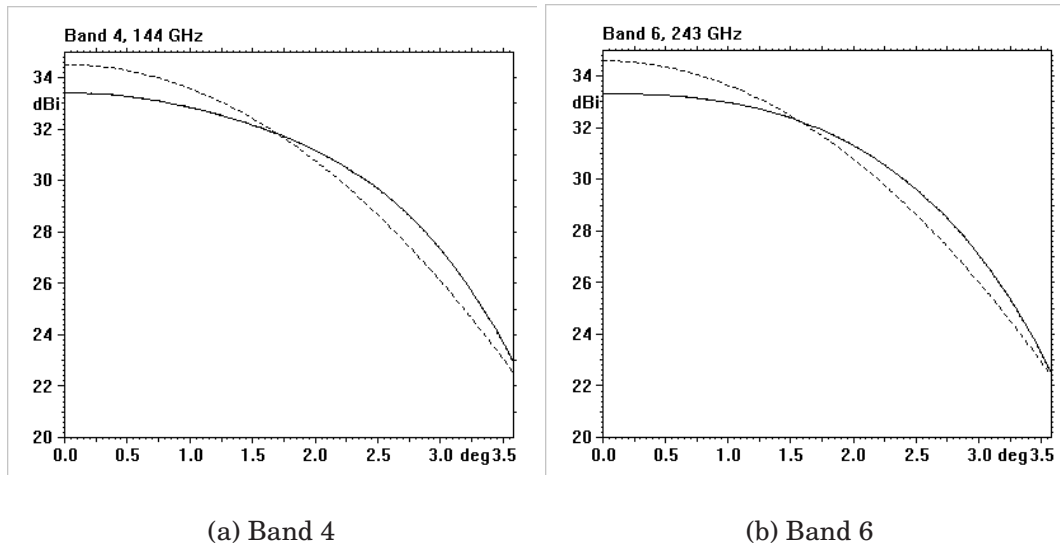
Table 5.1 Gaussian beam parameters.



(a) Band 3, 100 GHz

(b) Band 3, 116 GHz

Figure 5-1 Radiation patterns for front-end (full curve) and Gaussian beam feed (dotted curve).



(a) Band 4

(b) Band 6

Figure 5-2 Radiation patterns for front-end (full curve) and Gaussian beam feed (dotted curve).

In Figures 5-1 through 5-3 the patterns of the pertinent front-end are shown (x and y cuts) and compared to the pattern of the corresponding Gaussian feed (x cut only, since x and y cuts are identical).

Finally Table 5.2 lists all the calculated efficiencies.

<i>Band</i>	$\eta_{sp-over}$	η_{pol}	η_{amp}	η_{phase}	η_{tot}
Band 1, 31.3 GHz Gauss beam	0.9363	1.	0.8671	0.9996	0.8116
Band 2, 78 GHz Gauss beam	0.9252	1.	0.8800	1.	0.8142
Band 3, 100 GHz x-polarisation y-polarisation Gauss beam	0.9015 0.9015 0.9488	0.9993 0.9993 1.	0.8614 0.8614 0.8492	0.9934 0.9934 1.	0.7709 0.7709 0.8057
Band 3, 116 GHz x-polarisation y-polarisation Gauss beam	0.8895 0.8897 0.9489	0.9938 0.9937 1.	0.9208 0.9209 0.8490	0.9824 0.9827 1.	0.7997 0.8000 0.8056
Band 4, 144 GHz x-polarisation y-polarisation Gauss beam	0.9500 0.9500 0.9366	0.9983 0.9983 1.	0.9151 0.9151 0.8668	0.9995 0.9995 1.	0.8674 0.8674 0.8118
Band 5, 187 GHz Gauss beam	0.9369	1.	0.8663	1.	0.8117
Band 6, 243 GHz x-polarisation y-polarisation Gauss beam	0.9538 0.9538 0.9398	0.9996 0.9996 1.	0.9049 0.9049 0.8625	0.9996 0.9996 1.	0.8625 0.8625 0.8106
Band 7, 324 GHz x-polarisation y-polarisation Gauss beam	0.9370 0.9377 0.9399	0.9932 0.9932 1.	0.9018 0.9033 0.8624	0.9996 0.9995 1.	0.8389 0.8409 0.8106
Band 8, 442 GHz Gauss beam	0.9398	1.	0.8626	1.	0.8106
Band 9, 661 GHz x-polarisation y-polarisation Gauss beam	0.9332 0.9320 0.9386	0.9878 0.9878 1.	0.8959 0.8961 0.8641	0.9976 0.9975 1.	0.8239 0.8229 0.8111

Table 5.2 Efficiencies for front-ends.

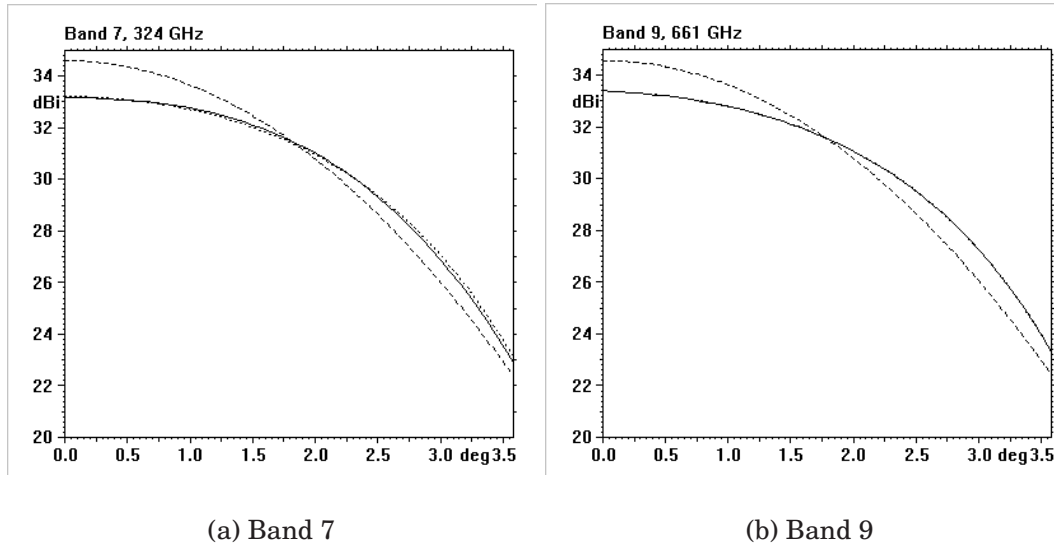


Figure 5-3 Radiation patterns for front-end (full curve) and Gaussian beam feed (dotted curve).

5.1.5 Conclusion.

When the results in Section 5.1.4 are compared to the requirements, it can be concluded that, at the centre frequencies of the bands, $\eta_{spill-over}$ exceeds 80% as required in all bands. Also $\eta_{taper} = \eta_{amplitude}\eta_{phase}$ exceeds the required 80% in all bands. However, $\eta_{polarisation}$ does not exceed 99.5% in Bands 7 and 9, but does so in all other bands. The total efficiency exceeds 80% as required in all bands, except Band 3.

5.2 Calculation of entire optical system beams

The far field from the entire optical system has now been calculated in a square region around the main beam. The width of the square region is around ± 5 times the 3-dB beamwidth at the centre frequency of each band.

For each band the front-end beams presented in Chapter 4 and gaussian beams have been used as source and located in the positions summarised in Table 5.3.

As a comparison the fundamental mode Gaussian beam has been extracted from the result of the gaussian mode analysis of the front-end optics and this gaussian beam has been used as a source for comparison. The data for these Gaussian beams are given in Table 5.4.

In all bands the pattern reference points are the same as the ones for the front-end patterns except for bands 3 and 4 where the axial movement ("Along axis in Table 5.3) has not been done for the

Band	(ρ ,z)	Azimuth	Tilt	Along axis
1	(255 mm, 0 mm)	135°	2.480°	270.253 mm
2	(255 mm, 0 mm)	-135°	2.480°	70.066 mm
3	(188 mm, 39 mm)	-80°	1.809°	64.77 mm
4	(196 mm, 39 mm)	80°	1.893°	245.11 mm
5	(245 mm, 0 mm)	-45°	2.38°	-15.013 mm
6	(245 mm, 0 mm)	45°	2.385°	-15.00 mm
7	(100 mm, 0 mm)	0°	0.970°	-50.01 mm
8	(100 mm, 0 mm)	-90°	1.010°	-50.008 mm
9	(100 mm, 0 mm)	90°	0.940°	-27.00 mm

Table 5.3 Reference positions for front-end patterns

Band	Frequency	Beam radius	Phase front radius
	GHz	mm	m
1	31.3	57.32	∞
2	78	22.29	∞
3	84	22.47	-2.598
3	100	18.91	-2.101
3	116	16.34	-1.718
4	125	19.50	-0.5408
4	144	18.15	-0.4689
4	163	16.98	-0.4191
5	187	9.599	∞
6	211	8.579	∞
6	243	7.449	∞
6	275	6.582	∞
7	275	6.584	∞
7	324	5.588	∞
7	373	4.854	∞
8	385	4.701	∞
8	442	4.095	∞
8	500	3.620	∞
9	602	2.996	∞
9	661	2.729	∞
9	720	2.505	∞

Table 5.4 Gaussian pattern parameters. For band 3 and 4 the Gaussian beam parameters refer to the centre of mirror 2

gaussian beams.

Prior to the calculations the position of the subreflector has been optimised by

- adjusting the subreflector tilt in the antenna axis-source plane so that the rays reflected in the subreflector hit the main reflector symmetrically around the central hole and
- moving the subreflector along the antenna axis so that the focus of an incoming plane wave reflected in main then sub falls at the position of the source (Table 5.3). The tilt/movement data for each band are listed in Table 5.5.

Band	Subreflector tilt	Subreflector axial shift
1	1.4°	0.85 mm
2	1.2°	0.26 mm
3	0.9°	0.32 mm
4	1.0°	0.90 mm
5	1.2°	-0.08 mm
6	1.2°	-0.06 mm
7	0.6°	-0.15 mm
8	0.5°	-0.20 mm
9	0.5°	-0.09 mm

Table 5.5 Subreflector position correction for each band - positive axial shift is away from main reflector

Calculation have been done assuming two polarisations: linear polarisation in the plane containing the source and the antenna axis (px) and linear polarisation perpendicular to this plane (py). In the calculations linear components in the same two planes have been retrieved.

The analysis has been done assuming 3 geometries:

- No struts
- AEM struts
- Vertex struts

In Table 5.6 the peak directivity values in band 1 are listed.

Frequency	Pol.	Source	No struts	AEM struts	Vertex struts	No struts, cross
31.3 GHz	px	Gauss	70.74 dBi	70.54 dBi	70.58 dBi	27.92 dBi
Average level of strut cases rel. to "no strut" cases			-0.20 dB		-0.16 dB	

Table 5.6 Peak directivity values for the band 1 frequency

In Table 5.7 the peak directivity values in band 3 in each of the

cases are listed.

Frequency	Pol.	Source	No struts	AEM struts	Vertex struts	No struts, cross
84 GHz	px	front-end	79.20 dBi	78.99 dBi	79.03 dBi	45.80 dBi
84 GHz	py	front-end	79.20 dBi	78.99 dBi	79.04 dBi	46.01 dBi
84 GHz	px	Gauss	79.38 dBi	79.17 dBi	79.22 dBi	33.80 dBi
100 GHz	px	front-end	80.76 dBi	80.56 dBi	80.60 dBi	45.69 dBi
100 GHz	py	front-end	80.77 dBi	80.57 dBi	80.61 dBi	45.76 dBi
100 GHz	px	Gauss	80.89 dBi	80.68 dBi	80.73 dBi	35.40 dBi
116 GHz	px	front-end	82.24 dBi	82.05 dBi	82.10 dBi	55.52 dBi
116 GHz	py	front-end	82.27 dBi	82.08 dBi	82.13 dBi	55.64 dBi
116 GHz	px	Gauss	82.19 dBi	81.98 dBi	82.04 dBi	36.67 dBi
Average level of strut cases rel. to "no strut" cases			-0.20 dB	-0.15 dB		

Table 5.7 Peak directivity values for band 3 frequencies

In Table 5.8 the peak directivity values in band 4 in each of the cases are listed.

Frequency	Pol.	Source	No struts	AEM struts	Vertex struts	No struts, cross
125 GHz	px	front-end	83.15 dBi	82.95 dBi	82.99 dBi	52.66 dBi
125 GHz	py	front-end	83.15 dBi	82.95 dBi	82.99 dBi	52.66 dBi
125 GHz	px	Gauss	82.87 dBi	82.65 dBi	82.70 dBi	37.72 dBi
144 GHz	px	front-end	84.10 dBi	84.20 dBi	84.23 dBi	53.45 dBi
144 GHz	py	front-end	84.10 dBi	84.20 dBi	84.23 dBi	53.44 dBi
144 GHz	px	Gauss	84.10 dBi	83.89 dBi	83.92 dBi	38.94 dBi
163 GHz	px	front-end	85.48 dBi	85.28 dBi	85.32 dBi	54.19 dBi
163 GHz	py	front-end	85.49 dBi	85.28 dBi	85.32 dBi	54.18 dBi
163 GHz	px	Gauss	85.17 dBi	84.96 dBi	85.00 dBi	40.02 dBi
Average level of strut cases rel. to "no strut" cases			-0.20 dB	-0.17 dB		

Table 5.8 Peak directivity values for band 4 frequencies

In Table 5.9 the peak directivity values in band 5 in each of the cases are listed.

Frequency	Pol.	Source	No struts	AEM struts	Vertex struts	No struts, cross
187 GHz	px	Gauss	86.38 dBi	86.17 dBi	86.21 dBi	43.26 dBi
Average level of strut cases rel. to "no strut" cases			-0.21 dB	-0.17 dB		

Table 5.9 Peak directivity values for band 5 frequency

In Table 5.10 the peak directivity values in band 6 in each of the cases are listed.

Frequency	Pol.	Source	No struts	AEM struts	Vertex struts	No struts, cross
211 GHz	px	front-end	87.66 dBi	87.47 dBi	87.52 dBi	53.15 dBi
211 GHz	py	front-end	87.67 dBi	87.47 dBi	87.52 dBi	53.18 dBi
211 GHz	px	Gauss	87.40 dBi	87.19 dBi	87.26 dBi	44.30 dBi
243 GHz	px	front-end	88.91 dBi	88.71 dBi	88.74 dBi	53.32 dBi
243 GHz	py	front-end	88.91 dBi	88.71 dBi	88.74 dBi	53.35 dBi
243 GHz	px	Gauss	88.63 dBi	88.42 dBi	88.45 dBi	45.48 dBi
275 GHz	px	front-end	90.00 dBi	89.80 dBi	89.83 dBi	53.54 dBi
275 GHz	py	front-end	90.00 dBi	89.80 dBi	89.83 dBi	53.57 dBi
275 GHz	px	Gauss	89.69 dBi	89.48 dBi	89.51 dBi	46.52 dBi
Average level of strut cases rel. to "no strut" cases			-0.20 dB	-0.16 dB		

Table 5.10 Peak directivity values for band 6 frequencies

In Table 5.11 the peak directivity values in band 7 in each of the cases are listed.

Frequency	Pol.	Source	No struts	AEM struts	Vertex struts	No struts, cross
275 GHz	px	front-end	89.83 dBi	89.63 dBi	89.67 dBi	66.63 dBi
275 GHz	py	front-end	89.85 dBi	89.65 dBi	89.69 dBi	66.69 dBi
275 GHz	px	Gauss	89.74 dBi	89.54 dBi	89.58 dBi	38.96 dBi
324 GHz	px	front-end	91.32 dBi	91.12 dBi	91.17 dBi	67.72 dBi
324 GHz	py	front-end	91.33 dBi	91.13 dBi	91.18 dBi	67.77 dBi
324 GHz	px	Gauss	91.17 dBi	90.96 dBi	91.02 dBi	40.41 dBi
373 GHz	px	front-end	92.59 dBi	92.39 dBi	92.43 dBi	68.75 dBi
373 GHz	py	front-end	92.59 dBi	92.39 dBi	92.44 dBi	68.77 dBi
373 GHz	px	Gauss	92.39 dBi	92.19 dBi	92.23 dBi	41.43 dBi
Average level of strut cases rel. to "no strut" cases			-0.20 dB	-0.15 dB		

Table 5.11 Peak directivity values for band 7 frequencies

In Table 5.12 the peak directivity values in band 8 in each of the cases (only Gaussian beams) are listed.

Frequency	Pol.	Source	No struts	AEM struts	Vertex struts	No struts, cross
385 GHz	px	Gauss	92.67 dBi	92.47 dBi	92.51 dBi	41.78 dBi
442 GHz	px	Gauss	93.87 dBi	93.67 dBi	93.71 dBi	43.02 dBi
500 GHz	px	Gauss	94.94 dBi	94.74 dBi	94.78 dBi	44.01 dBi
Average level of strut cases rel. to "no strut" cases			-0.20 dB	-0.16 dB		

Table 5.12 Peak directivity values for band 8 frequencies

In Table 5.13 the peak directivity values in band 9 in each of the

cases are listed.

Frequency	Pol.	Source	No struts	AEM struts	Vertex struts	No struts, cross
602 GHz	px	front-end	96.60 dBi	96.40 dBi	96.44 dBi	75.31 dBi
602 GHz	py	front-end	96.60 dBi	96.40 dBi	96.44 dBi	75.34 dBi
602 GHz	px	Gauss	96.56 dBi	96.35 dBi	96.39 dBi	45.72 dBi
661 GHz	px	front-end	97.45 dBi	97.25 dBi	97.27 dBi	76.09 dBi
661 GHz	py	front-end	97.44 dBi	97.24 dBi	97.26 dBi	76.12 dBi
661 GHz	px	Gauss	97.36 dBi	97.16 dBi	97.18 dBi	46.57 dBi
720 GHz	px	front-end	98.21 dBi	98.01 dBi	98.02 dBi	76.82 dBi
720 GHz	py	front-end	98.20 dBi	98.00 dBi	98.02 dBi	76.83 dBi
720 GHz	px	Gauss	98.11 dBi	97.90 dBi	97.91 dBi	47.26 dBi
Average level of strut cases rel. to "no strut" cases			-0.20 dB	-0.17 dB		

Table 5.13 Peak directivity values for band 9 frequencies

In Table 5.14 a comparison between the Gaussian (fundamental-mode) beam and the beam coming out of the analysis of the front-end is done by comparing the peak levels of the far field from the complete antenna.

Band	Frequency	Gauss rel. to front-end
3	84 GHz	+0.18 dB
3	100 GHz	+0.13 dB
3	116 GHz	-0.06 dB
4	125 GHz	-0.29 dB
4	144 GHz	-0.31 dB
4	163 GHz	-0.32 dB
6	211 GHz	-0.27 dB
6	243 GHz	-0.29 dB
6	275 GHz	-0.32 dB
7	275 GHz	-0.09 dB
7	324 GHz	-0.15 dB
7	373 GHz	-0.20 dB
9	602 GHz	-0.05 dB
9	661 GHz	-0.09 dB
9	720 GHz	-0.11 dB

Table 5.14 Level of far field beam peak when using Gaussian feed as source relative to level when using calculated front-end beams (positive values mean "Gaussian is better") - average for "no struts", "AEM struts" and "Vertex struts"

It is seen that in most of the cases the peak level obtained using the Gaussian beam as the source is lower than the peak level

obtained by using the front-end pattern as source. To illustrate the reason for this the far field pattern of the Gaussian beam has been compared to the far field pattern of the analysed front-end design. Furthermore, the field distribution on the surface of the subreflector using these two source models has been compared in the following graphs by means of a surface cut through the telescope axis.

In Figures 5-4 and 5-5 this comparison has been done at 100 GHz. In Figure 5-4 the black curve indicates the Gaussian beam (rotationally symmetric), the full red curve indicates the front-end field in the plane containing the source and the telescope axis (positive angles away from axis) and the dashed red curve indicates the field in the plane perpendicular to that.

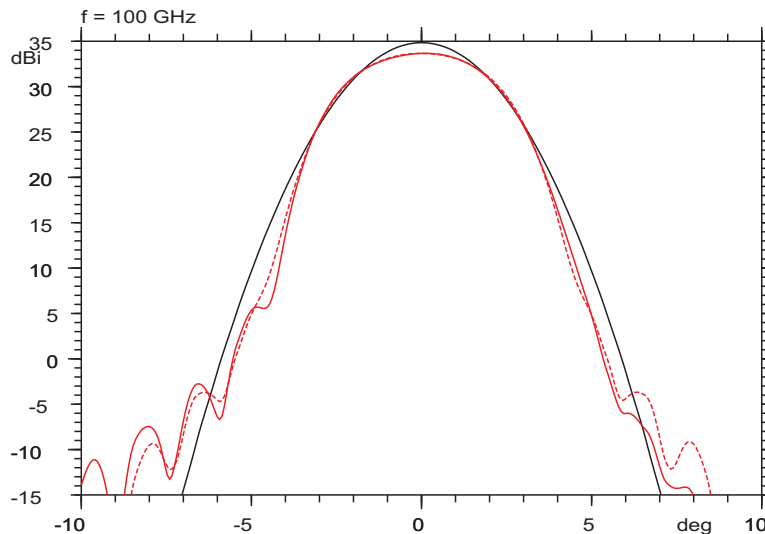


Figure 5-4 Farfield from Gaussian fundamental mode and from associated front-end at 100 GHz

In Figure 5-5 the black curves indicate the subreflector surface field coming from the Gaussian beam and the red curves the subreflector surface field from the front-end beam. The full curves are in the plane containing the source and the dashed curves are in the perpendicular plane where the Gaussian pattern will be symmetric.

The general trend is that the peak of the Gaussian pattern is higher than that of the front-end beam, however, the front-end beam is wider so that a greater percentage of the power is hitting the subreflector which will give rise to a higher peak of the far field beam from the telescope. In the "100 GHz" case the Gaussian beam is "a little bit better" according to Table 5.14. This is in agreement with the pattern in Figure 5-5 where the "front-end" field is only slightly higher than the "Gaussian" field in the zone around 250 mm from the telescope axis. In Figures 5-7, 5-9, 5-11 and 5-13 the "front-end" field is considerably higher than the "Gaussian" field in this region, hence, more power is incident on the subreflector and the telescope far field beam is higher.

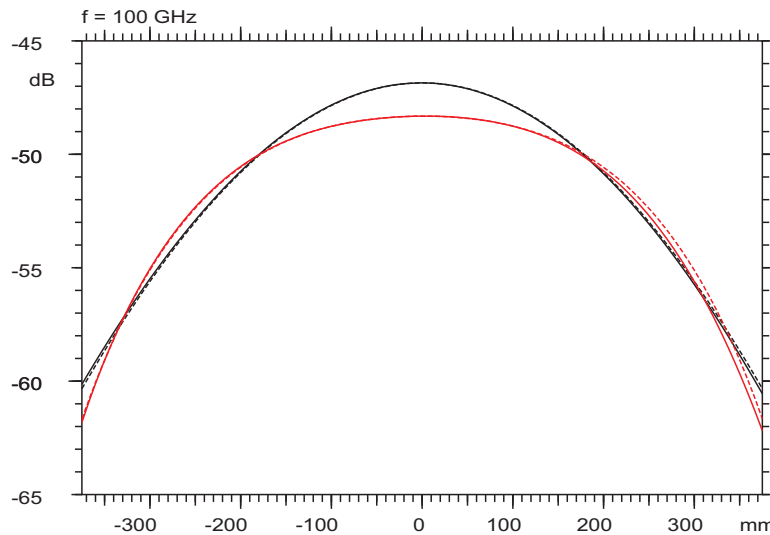


Figure 5-5 Subreflector aperture field from Gaussian fundamental mode and from associated front-end at 100 GHz

In Figures 5-6 and 5-7 the same comparison has been made at 144 GHz.

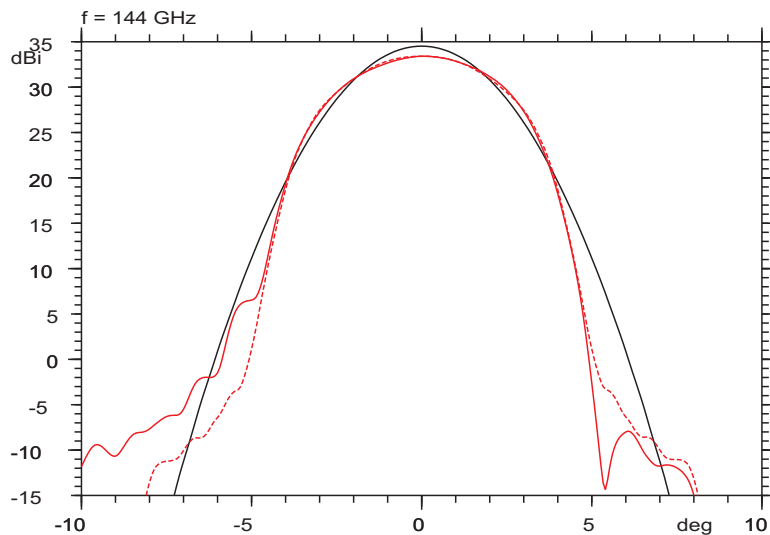


Figure 5-6 Farfield from Gaussian fundamental mode and from associated front-end at 144 GHz

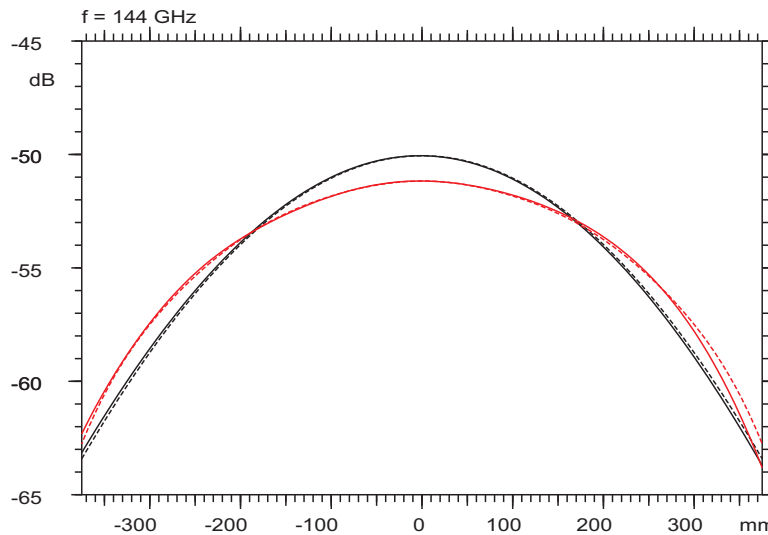


Figure 5-7 Subreflector aperture field from Gaussian fundamental mode and from associated front-end at 144 GHz

In Figures 5-8 and 5-9 the same comparison has been made at 243 GHz.

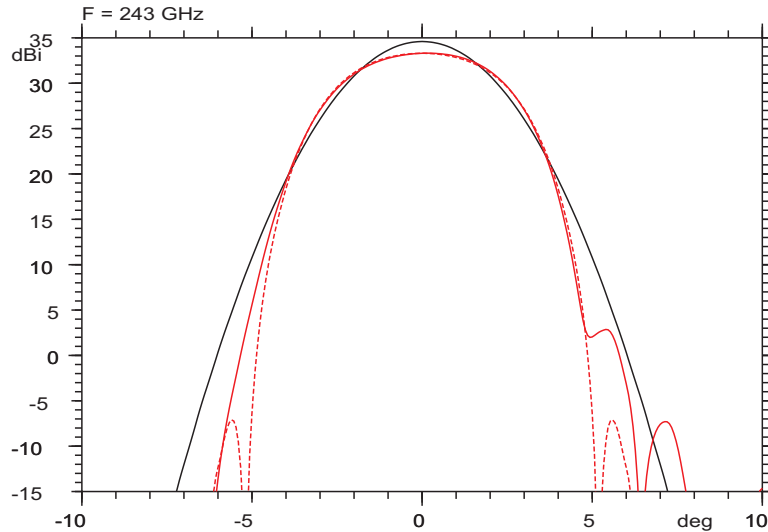


Figure 5-8 Farfield from Gaussian fundamental mode and from associated front-end at 243 GHz

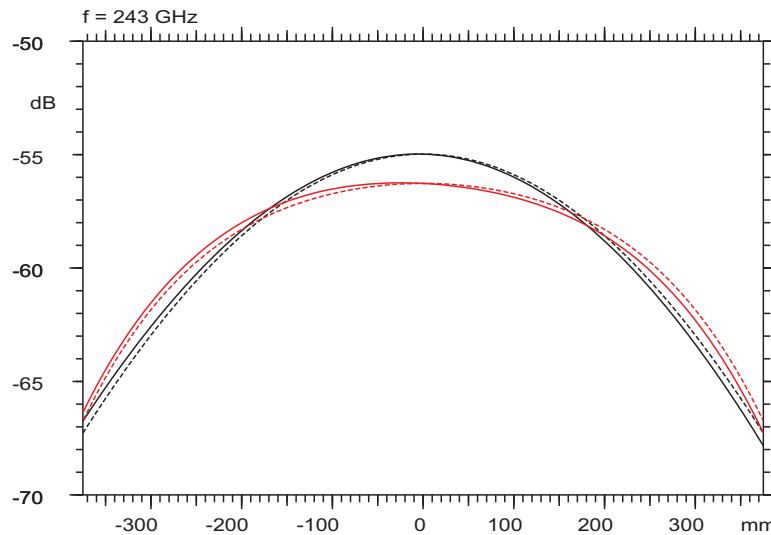


Figure 5-9 Subreflector aperture field from Gaussian fundamental mode and from associated front-end at 243 GHz

In Figures 5-10 and 5-11 the same comparison has been made at 324 GHz.

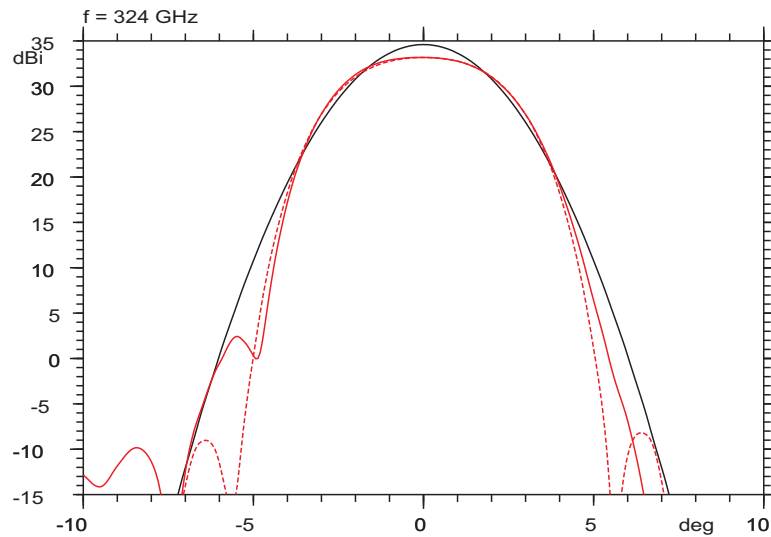


Figure 5-10 Farfield from Gaussian fundamental mode and from associated front-end at 324 GHz

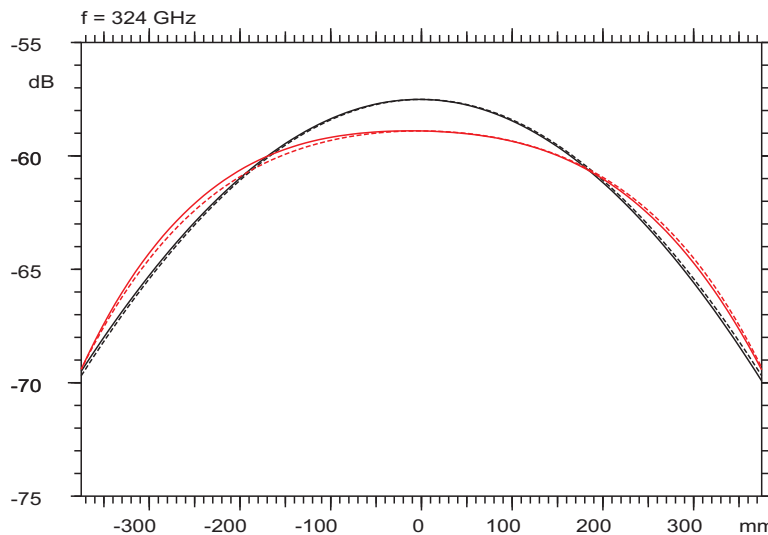


Figure 5-11 Subreflector aperture field from Gaussian fundamental mode and from associated front-end at 324 GHz

In Figures 5-12 and 5-13 the same comparison has been made at 661 GHz.

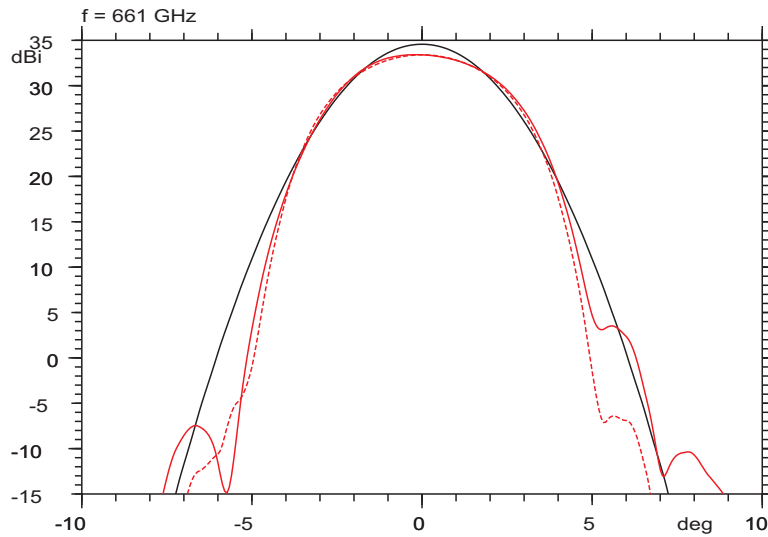


Figure 5-12 Farfield from Gaussian fundamental mode and from associated front-end at 661 GHz

The field from the entire optics has been calculated as described in the beginning of this section and a contour plot of the copolar component is shown in Figure 5-14 in the case of $f = 243$ GHz and assuming no struts.

The cross polar component looks as shown in Figure 5-15.

The calculation has been repeated with the AEM struts included in the analysis. The result is shown in Figures 5-16 (copolar) and 5-17 (cross polar).

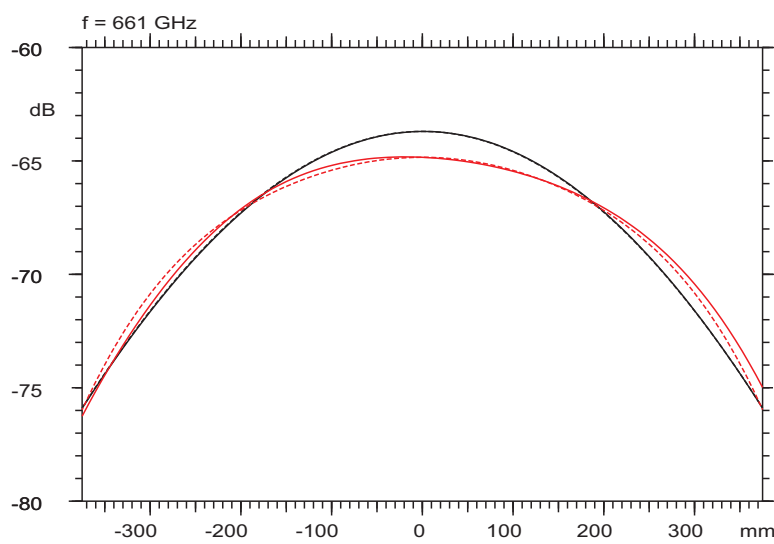


Figure 5-13 Subreflector aperture field from Gaussian fundamental mode and from associated front-end at 661 GHz

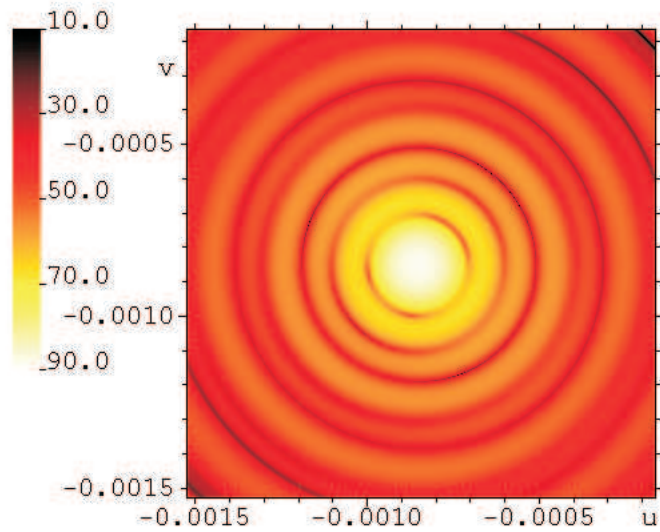


Figure 5-14 Copolar farfield from entire optical system assuming no struts at 243 GHz, px polarisation, front-end data - maximum directivity 88.91 dBi

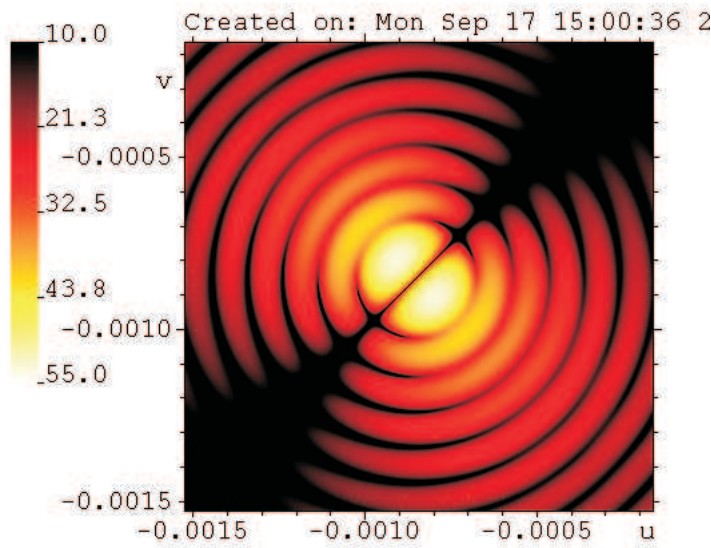


Figure 5-15 Cross polar farfield from entire optical system assuming no struts at 243 GHz, px polarisation, front-end data - maximum directivity 53.32 dBi

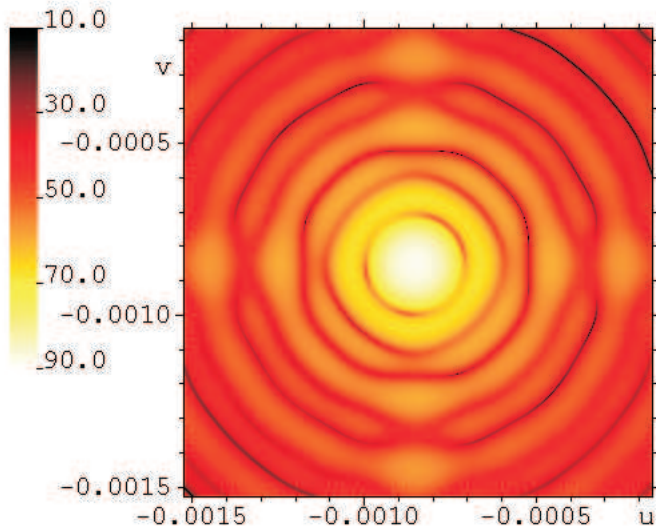


Figure 5-16 Copolar farfield from entire optical system assuming AEM struts at 243 GHz, px polarisation, front-end data - maximum directivity 88.71 dBi

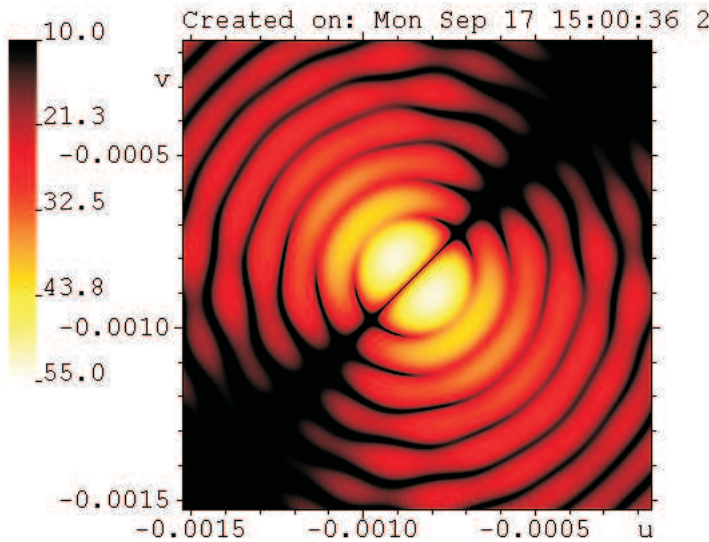


Figure 5-17 Cross polar farfield from entire optical system assuming AEM struts at 243 GHz, px polarisation, front-end data - maximum directivity 53.16 dBi

Finally, the calculation has been done with the Vertex struts included in the analysis. The result is shown in Figures 5-18 (copolar) and 5-19 (cross polar).

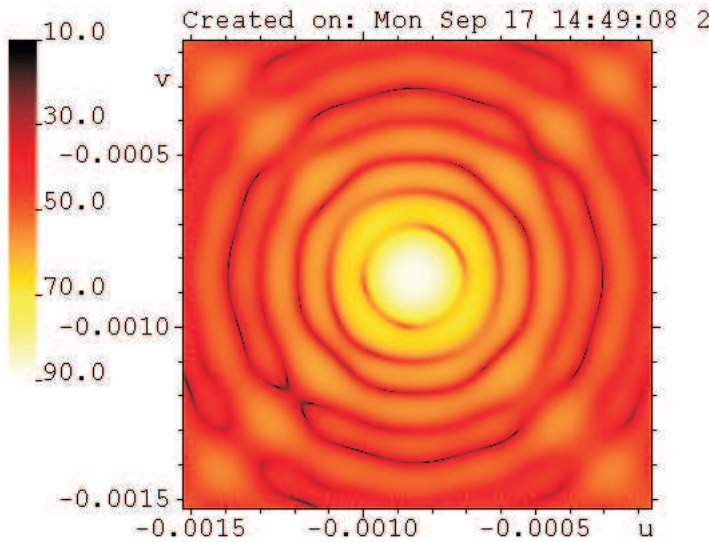


Figure 5-18 Copolar farfield from entire optical system assuming Vertex struts at 243 GHz, px polarisation, front-end data - maximum directivity 88.74 dBi

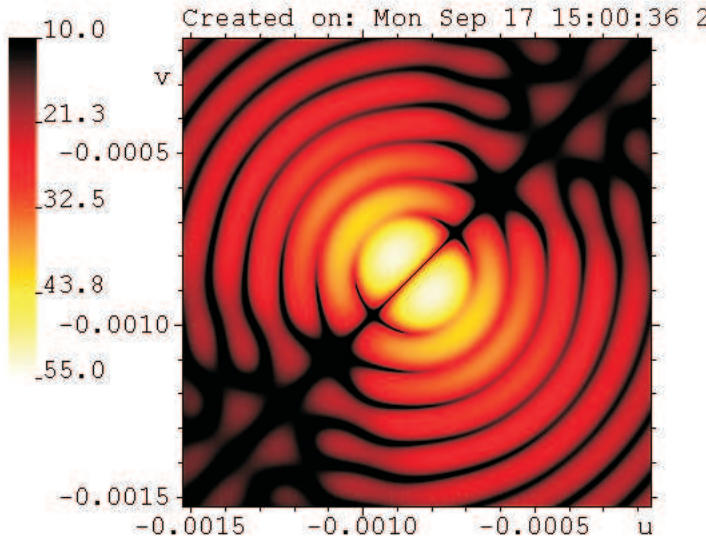


Figure 5-19 Cross polar farfield from entire optical system assuming Vertex struts at 243 GHz, px polarisation, front-end data - maximum directivity 53.21 dBi

Presented as pattern cuts a comparison has now been made between the farfield assuming no struts, AEM struts and Vertex struts. The result is shown in Figure 5-20 as regards the $\phi = 0.0^\circ$ plane (containing two AEM struts). Due to the fact that this plane contains two AEM struts the AEM strut field is significantly different from the "no struts" field whereas the "Vertex struts" pattern is closer to the "no struts" pattern.

In Figure 5-21 the same comparison is done in the $\phi = 45.0^\circ$ plane (containing two Vertex struts). For the same reason as above the Vertex pattern is now most different from the "no struts" pattern.

In Figure 5-22 the comparison is done in the $\phi = 90.0^\circ$ plane (containing two AEM struts). Again the AEM pattern is most different from the "no struts" pattern.

Finally, in Figure 5-23 the comparison is done in the $\phi = 135.0^\circ$ plane (containing two Vertex struts) showing the same situation as in Figure 5-21.

5.2.1 File name convention

For all the cases presented in the tables above field data for generating contour plots are provided in files. The name of the files describe the content in the following way:

`band{integer1}_f{integer2}_p{string1}_{string2}Struts_{string3}_uv.grd`

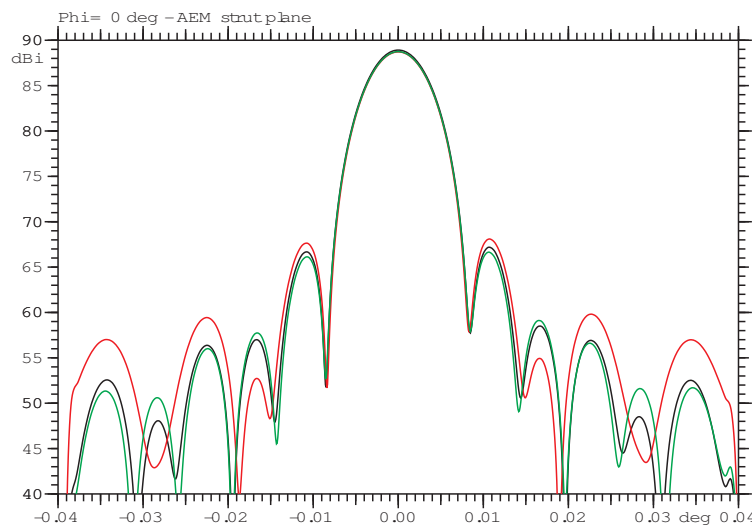


Figure 5-20 Copolar farfield from entire optical system assuming No struts (black), AEM struts (red) and Vertex struts (green) at 243 GHz, px polarisation, front-end data - phi = 0 degrees (AEM strut plane)

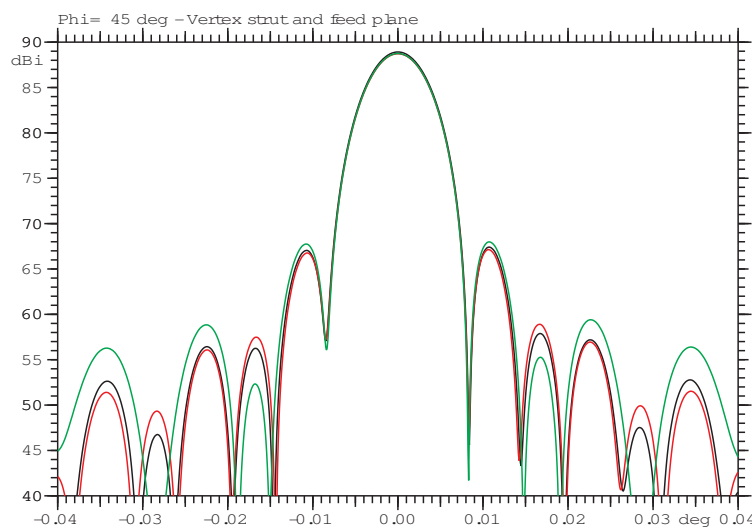


Figure 5-21 Copolar farfield from entire optical system assuming No struts (black), AEM struts (red) and Vertex struts (green) at 243 GHz, px polarisation, front-end data - phi = 45 degrees (Vertex strut plane and source plane)

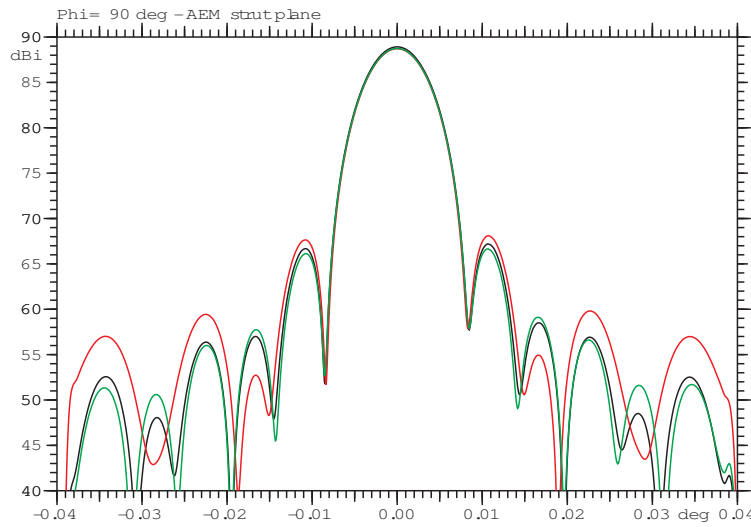


Figure 5-22 Copolar farfield from entire optical system assuming No struts (black), AEM struts (red) and Vertex struts (green) at 243 GHz, px polarisation, front-end data - phi = 90 degrees (AEM strut plane)

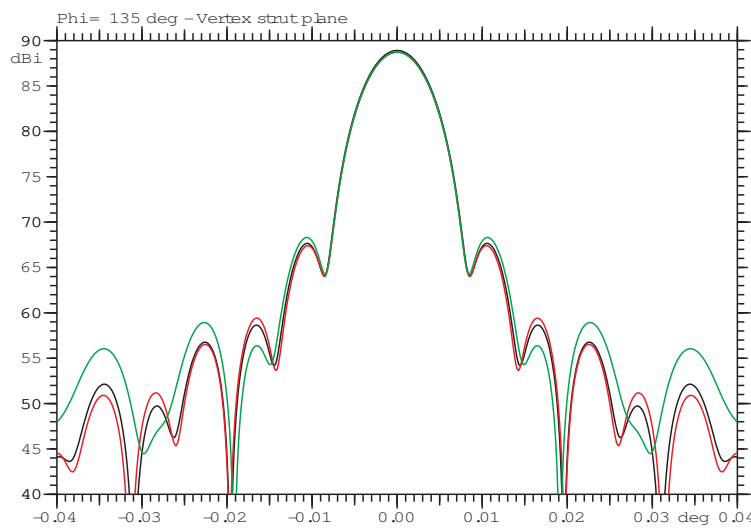


Figure 5-23 Copolar farfield from entire optical system assuming No struts (black), AEM struts (red) and Vertex struts (green) at 243 GHz, px polarisation, front-end data - phi = 0 degrees (Vertex strut plane)

f=100 GHz (band 3) $\tau=0.0375$; $T_{atm,n}=9.7\text{K}$; $T_{rec}=32\text{K}$						
Feed dep.	G	P_m	P_u	P_{gr}	T_{tot}	G/T
0.0 mrad	80.89	0.9473	0.0468	0.0059	43.230	64.532
1.0 mrad	80.89	0.9473	0.0468	0.0059	43.230	64.532
1.5 mrad	80.89	0.9473	0.0469	0.0059	43.204	64.535

Table 5.15 Impact on G/T of source depointing

f=144 GHz (band 4) $\tau=0.0438$; $T_{atm,n}=11.3\text{K}$; $T_{rec}=51\text{K}$						
Feed dep.	G	P_m	P_u	P_{gr}	T_{tot}	G/T
0.0 mrad	84.10	0.9472	0.0483	0.0045	63.460	66.075
1.0 mrad	84.10	0.9474	0.0482	0.0044	63.434	66.077
1.5 mrad	84.10	0.9475	0.0483	0.0042	63.382	66.080

Table 5.16 Impact on G/T of source depointing

where

integer1 indicates the band number (1 through 10)

integer2 indicates the frequency in GHz

string1 is "x" if polarisation is in the plane containing telescope axis and source and it is "y" if it is perpendicular to that plane

string2 is "No" if struts are not included in the analysis, it is "AEM" if it is AEM struts and it is "Vertex" if it is Vertex struts

string3 is "Gauss" if theoretical Gauss parameters are used for the source and it is "FrEnd" if the result of front end analysis is used for the source.

5.3 Calculation of aperture efficiency and G/T

Following the procedure in Section 3.1.3 the G/T calculation have been done at one frequency in 5 bands for a realistic pointing error of the source. Common to all cases is that the selected source pointing error gives rise to almost no change in the G/T . In order to investigate how much source pointing error is "needed" in order to give rise to serious G/T degradation, larger source depointing values have been included in the analysis in Band 6 (5.17). It shows that depointing values up to 5 mrad can be tolerated.

f=243 GHz (band 6) $\tau=0.0598$; $T_{atm,n}=15.3\text{K}$; $T_{rec}=55\text{K}$						
Feed dep.	G	P_m	P_u	P_{gr}	T_{tot}	G/T
0.0 mrad	88.63	0.9354	0.0617	0.0029	71.036	70.115
1.0 mrad	88.63	0.9349	0.0622	0.0029	71.036	70.115
1.5 mrad	88.63	0.9346	0.0625	0.0029	71.036	70.115
5.0 mrad	88.58	0.9306	0.0667	0.0027	70.985	70.068
10.0 mrad	88.45	0.9191	0.0780	0.0029	71.036	69.935
20.0 mrad	87.96	0.8749	0.1215	0.0036	71.213	69.434

Table 5.17 Impact on G/T of source depointing

f=324 GHz (band 7) $\tau=0.1239$; $T_{atm,n}=30.8\text{K}$; $T_{rec}=75\text{K}$						
Feed dep.	G	P_m	P_u	P_{gr}	T_{tot}	G/T
0.0 mrad	91.17	0.9346	0.0631	0.0023	106.348	70.903
1.0 mrad	91.17	0.9346	0.0631	0.0023	106.348	70.903
1.5 mrad	91.17	0.9345	0.0631	0.0024	106.372	70.902

Table 5.18 Impact on G/T of source depointing

f=442 GHz (band 8) $\tau=0.5350$; $T_{atm,n}=109.3\text{K}$; $T_{rec}=196\text{K}$						
Feed dep.	G	P_m	P_u	P_{gr}	T_{tot}	G/T
0.0 mrad	93.87	0.9349	0.0633	0.0018	305.587	69.019

Table 5.19 G/T figure at one frequency in band 8

f=661 GHz (band 9) $\tau=1.3203$; $T_{atm,n}=193.4\text{K}$; $T_{rec}=140\text{K}$						
Feed dep.	G	P_m	P_u	P_{gr}	T_{tot}	G/T
0.0 mrad	97.36	0.9355	0.0630	0.0015	333.513	72.129

Table 5.20 G/T figure at 661 GHz in band 9

f=720 GHz (band 9) $\tau=1.3334$; $T_{atm,n}=194.3\text{K}$; $T_{rec}=140\text{K}$						
Feed dep.	G	P_m	P_u	P_{gr}	T_{tot}	G/T
0.0 mrad	98.11	0.9358	0.0630	0.0012	334.390	72.867

Table 5.21 G/T figure at 720 GHz in band 9

5.4 Reflector deformations and beam performance

5.4.1 Presentation of the geometrical surface deformations

The main reflector surface will deform due to gravitation, wind and thermal gradients. Examples of all three types of distortions have been provided to TICRA. In each case the deformation is defined by means of two files. In the first file the nominal position in x , y and z of a number of points on the reflector are listed. In the second file the deformation is given by the deviation of the same points in x , y and z . This is sufficient to define the reflector surface shape.

It should be noted that the deformations provided are related to the support structure, but it assumed that they will be directly transferred to the reflector surface.

5.4.1.1 Deformations for the AEM antenna

First the deformations due to gravitation for 0° elevation is considered. Figure 5-24 shows the deformed surface relative to the nominal paraboloid. The unit on the z -axis is mm. It is seen that there is significant difference, in the order of 0.5 mm at the edge.

From the deformed surface it is possible to find a best fit paraboloid. It has six degrees of freedom: the vertex position in x , y and z , the focal length and the axis direction. TICRA uses an iterative method to determine the best fit paraboloid whereas AEM uses a deterministic approach. It has been checked that the two methods give exactly the same result.

Figure 5-25 shows the best fit paraboloid relative to the nominal paraboloid and it is seen that most of the deviations in Figure 5-24 are very well represented by the best fit paraboloid. In other words, the reflector deformations change the nominal paraboloid into another paraboloid. Figure 5-26 shows the remaining surface errors as the difference between the real deformed surface and the best fit paraboloid. The maximum deviation is here only about $50\mu\text{m}$ and the rms error has been calculated to $12\mu\text{m}$.

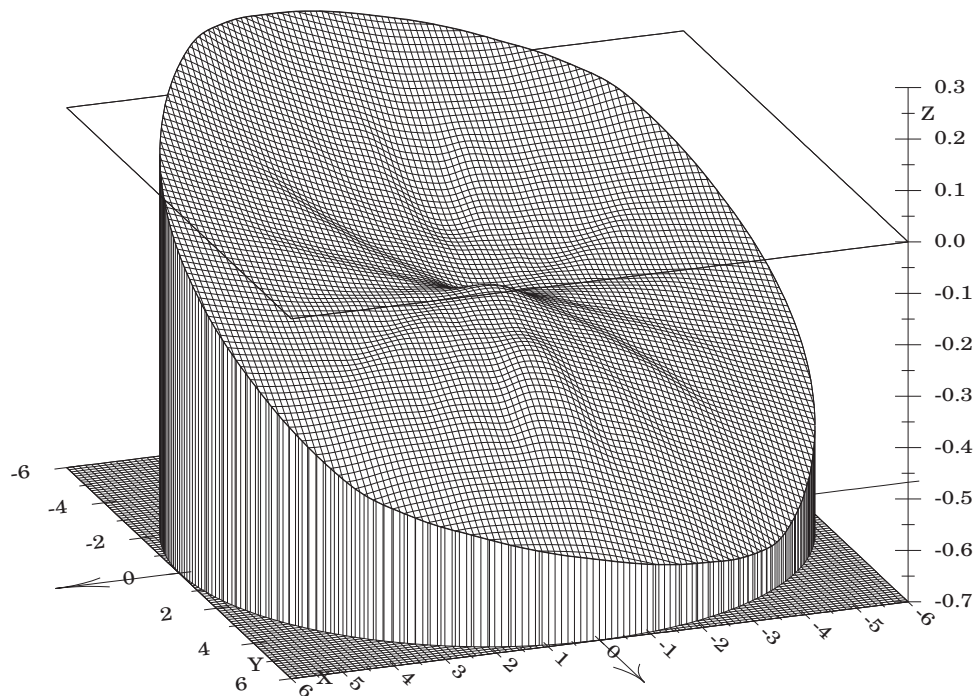


Figure 5-24 The deviation between the nominal paraboloid and the deformed reflector, 0° elevation.

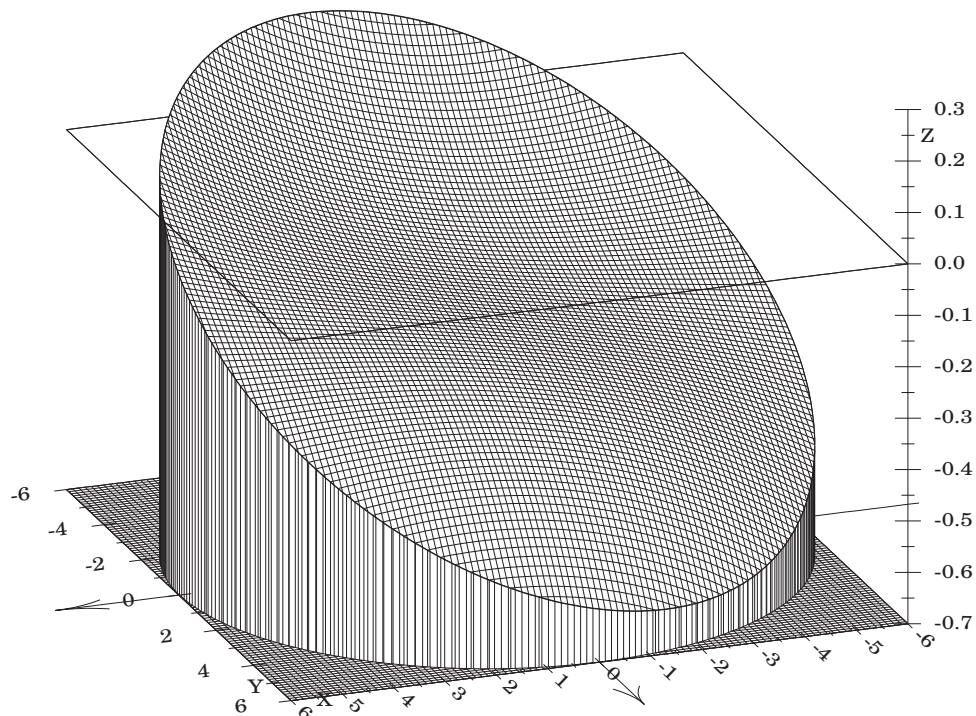


Figure 5-25 The deviation between the nominal and the best fit paraboloid.

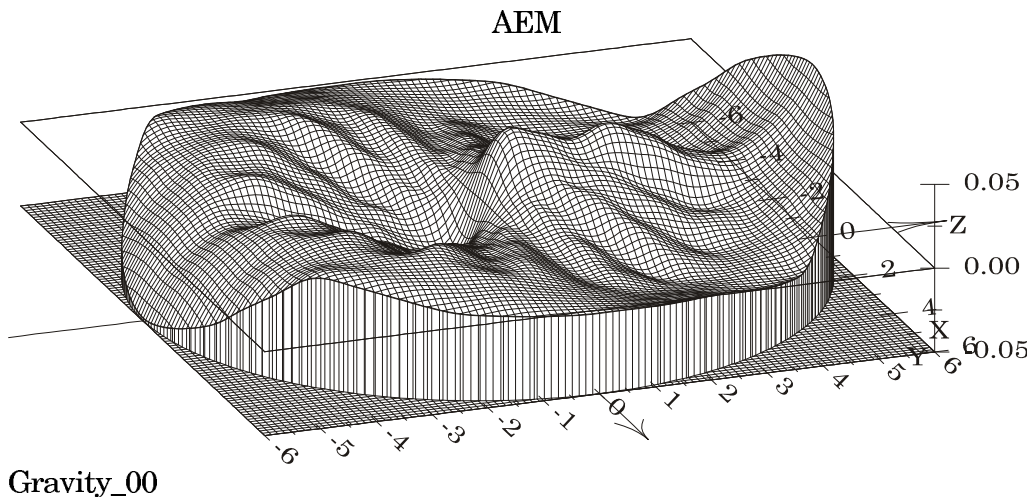


Figure 5-26 The deviation between the deformed reflector and the best fit paraboloid.

Figures 5-27 and 5-28 show the deviation between the deformed reflector and the best fit paraboloid for the elevation angles $15^\circ, 30^\circ, 45^\circ, 60^\circ, 75^\circ$ AND 90° . It is clearly seen that there is a very gradual change from 0° elevation to 90° elevation.

Figure 5-29 shows three additional cases:

top: a temperature variation of 10°C in the y -direction (this case is abbreviated "GY")

middle: a temperature change of 20°C of the complete antenna (this case is abbreviated "T20")

bottom: a wind load case (this case is abbreviated "W06")

The results in Figure 5-29 show that the temperature gradient and the wind case have very small influence on the reflector shape whereas the uniform temperature change, "T20", has a noticeable influence.

The results for the best fit paraboloid are summarized in Figure 5-30, indicating the focal length, the vertex position and the direction of the best fit paraboloid axis. The right column in the table shows the rms value of the ray path length error due to the reflector deformations. This number is approximately twice the rms error of the reflector surface shape.

For the RF calculations for the AEM antenna to be presented in Section 5.4.3 the four most interesting cases have been selected: gravitation for the elevation angles $0^\circ, 45^\circ$ and 90° and the uniform temperature case, "T20".

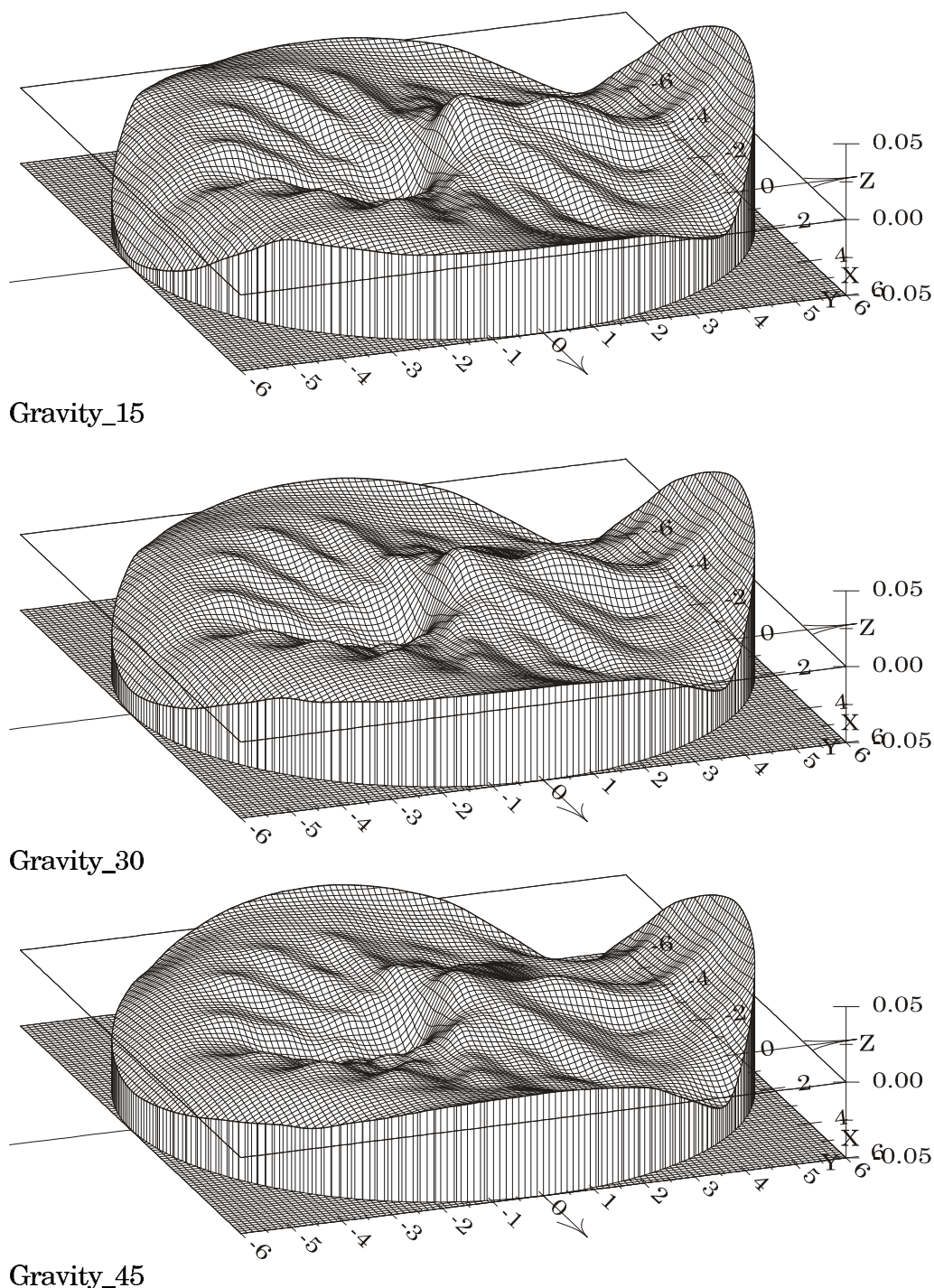


Figure 5-27 The deviation between the deformed reflector and the best fit paraboloid.

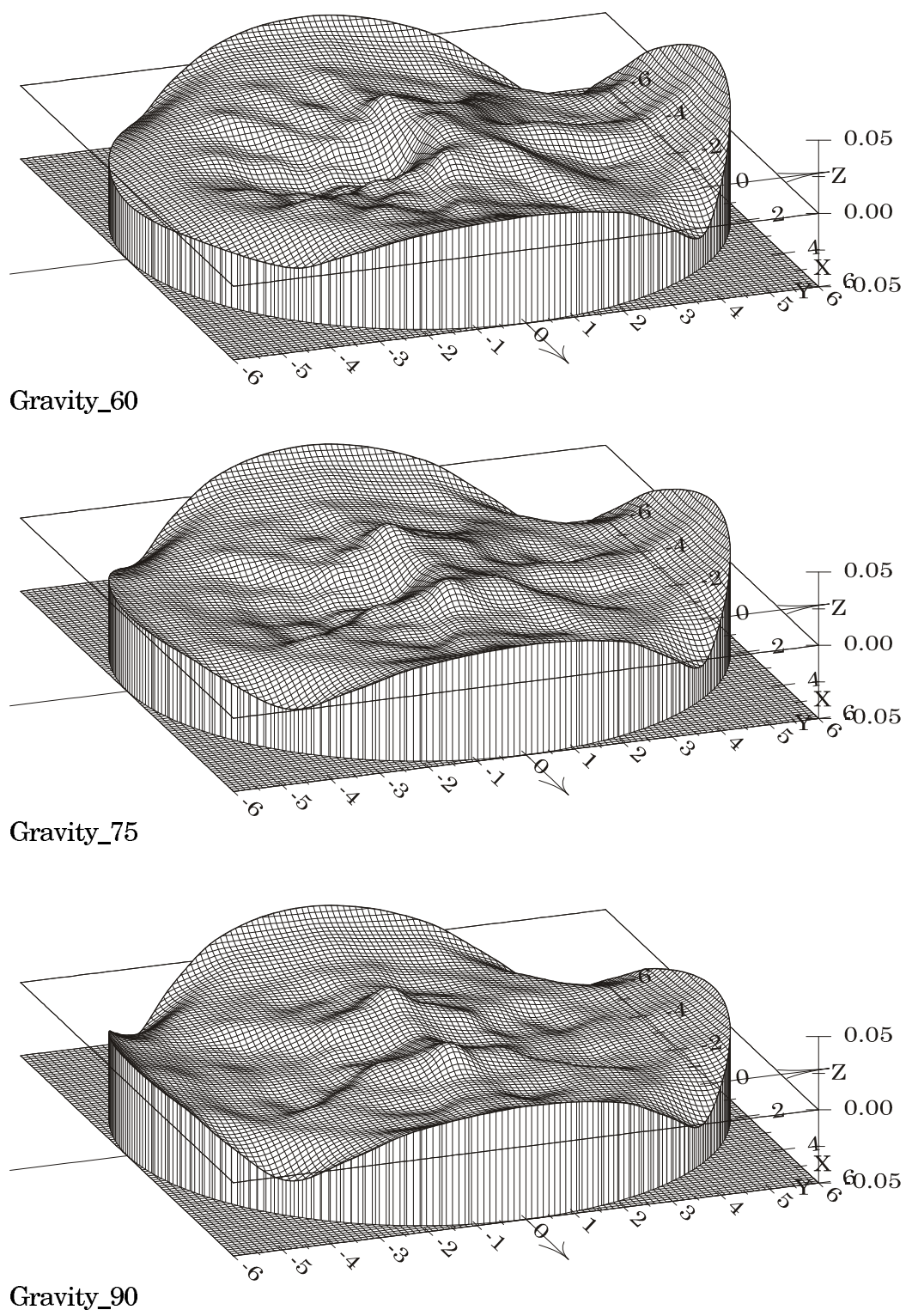


Figure 5-28 The deviation between the deformed reflector and the best fit paraboloid.

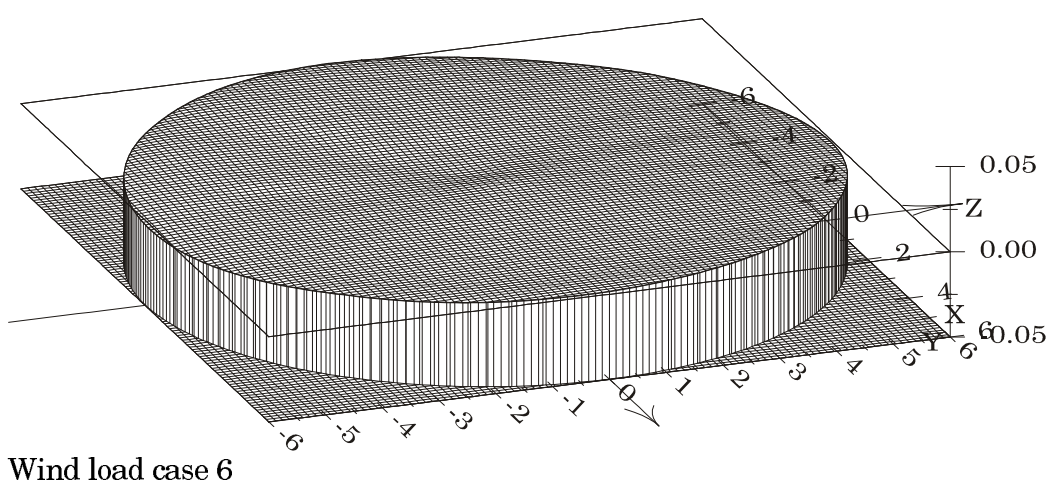
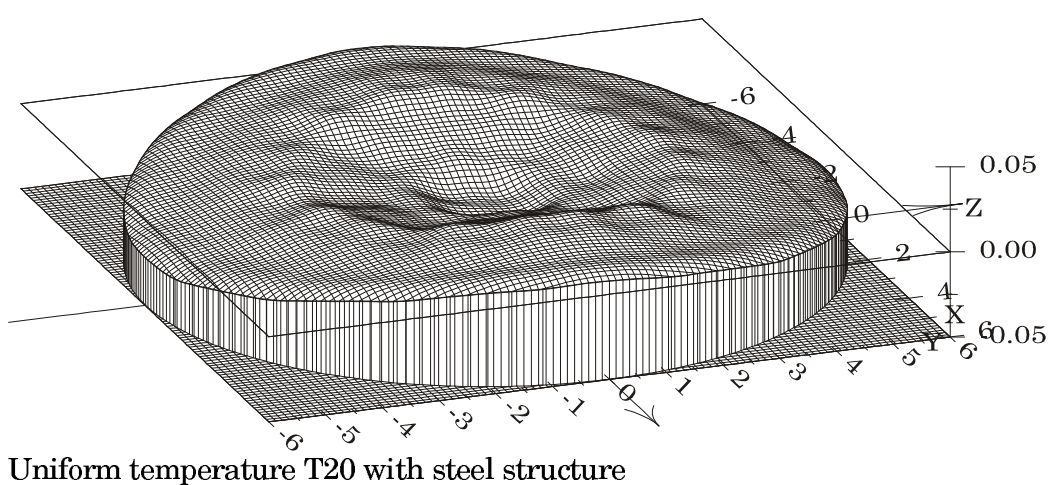
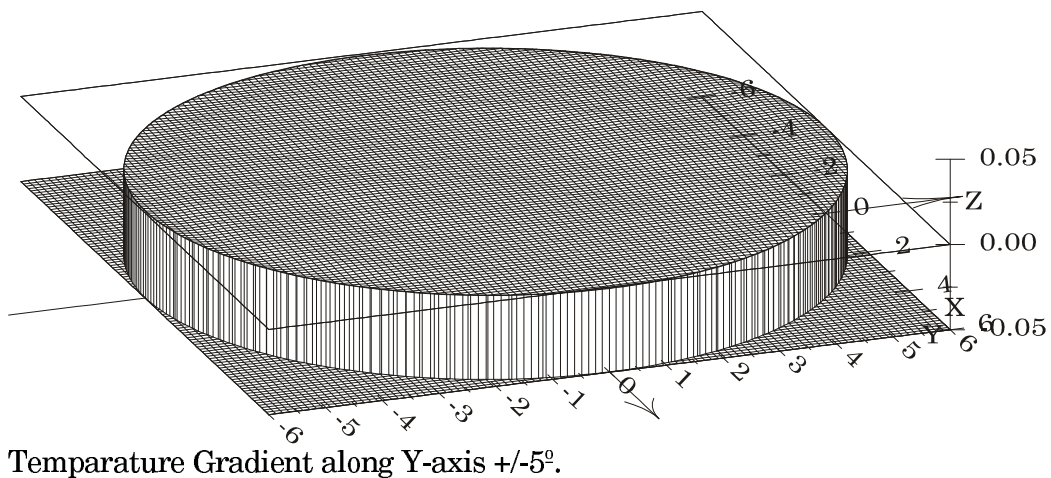


Figure 5-29 The deviation between the deformed reflector and the best fit paraboloid.

Surface distortions	focal length		Vertex			Main axis rotation		Aperture
	change	change	x	y	z	around x	around y	rms
	mm	df/F	mm	mm	mm	mRadians	mRadians	mm
AEM								
gravity cases								
elevation angles								
0°	-0.0054	-1.128E-06	-0.0372	-1.8028	-0.2234	-0.2097	-0.0166	0.0240
15°	0.0687	1.431E-05	-0.0369	-1.7960	-0.3092	-0.2018	-0.0167	0.0234
30°	0.1393	2.903E-05	-0.0331	-1.6797	-0.3701	-0.1753	-0.0149	0.0218
45°	0.1997	4.160E-05	-0.0275	-1.4493	-0.4065	-0.1391	-0.0123	0.0195
60°	0.2466	5.138E-05	-0.0203	-1.1196	-0.4165	-0.0919	-0.0084	0.0169
75°	0.2759	5.748E-05	-0.0140	-0.7157	-0.3959	-0.0370	-0.0043	0.0143
90°	0.2876	5.992E-05	-0.0044	-0.2636	-0.3509	0.0226	0.0002	0.0135
Thermal cases								
gy	-0.0006	-1.294E-07	0.0000	0.0202	0.0001	-0.0001	0.0000	0.0007
t20	-0.1125	-2.344E-05	-0.0120	0.0428	2.1310	-0.0061	-0.0013	0.0140
Wind case								
w06	-0.0098	-2.040E-06	-0.0365	-0.0141	0.0101	-0.0071	0.0093	0.0023

Figure 5-30 The parameters for the best fit paraboloid.

5.4.1.2 Deformations for the Vertex antenna

The information about the surface deformations for the Vertex antenna has been provided to TICRA in almost the same format as for the AEM antenna and the determination of the best fit paraboloid has been carried out in the same way. A total of 14 cases have been provided and the best fit paraboloid parameters are summarised in the table in Figure 5-34. The nine most interesting cases are illustrated in the following plots.

Figure 5-31 shows the deviation between the gravity deformed reflector and the best fit paraboloid for the elevation angles 0°, 50° and 90°.

Figure 5-32 shows three wind cases. The influence from the wind is seen to be quite small.

Figure 5-33 shows three temperature cases. The plots show that the most serious impact happens for a uniform change of the temperature of 20°.

For the RF calculations for the Vertex antenna to be presented in Section 5.4.4 the five most interesting cases have been selected: gravitation for the elevation angles 0°, 50° and 90°, the side wind from 50° for 0° elevation (the lower plot in Figure 5-32) and the uniform temperature case (the lower plot in Figure 5-33).

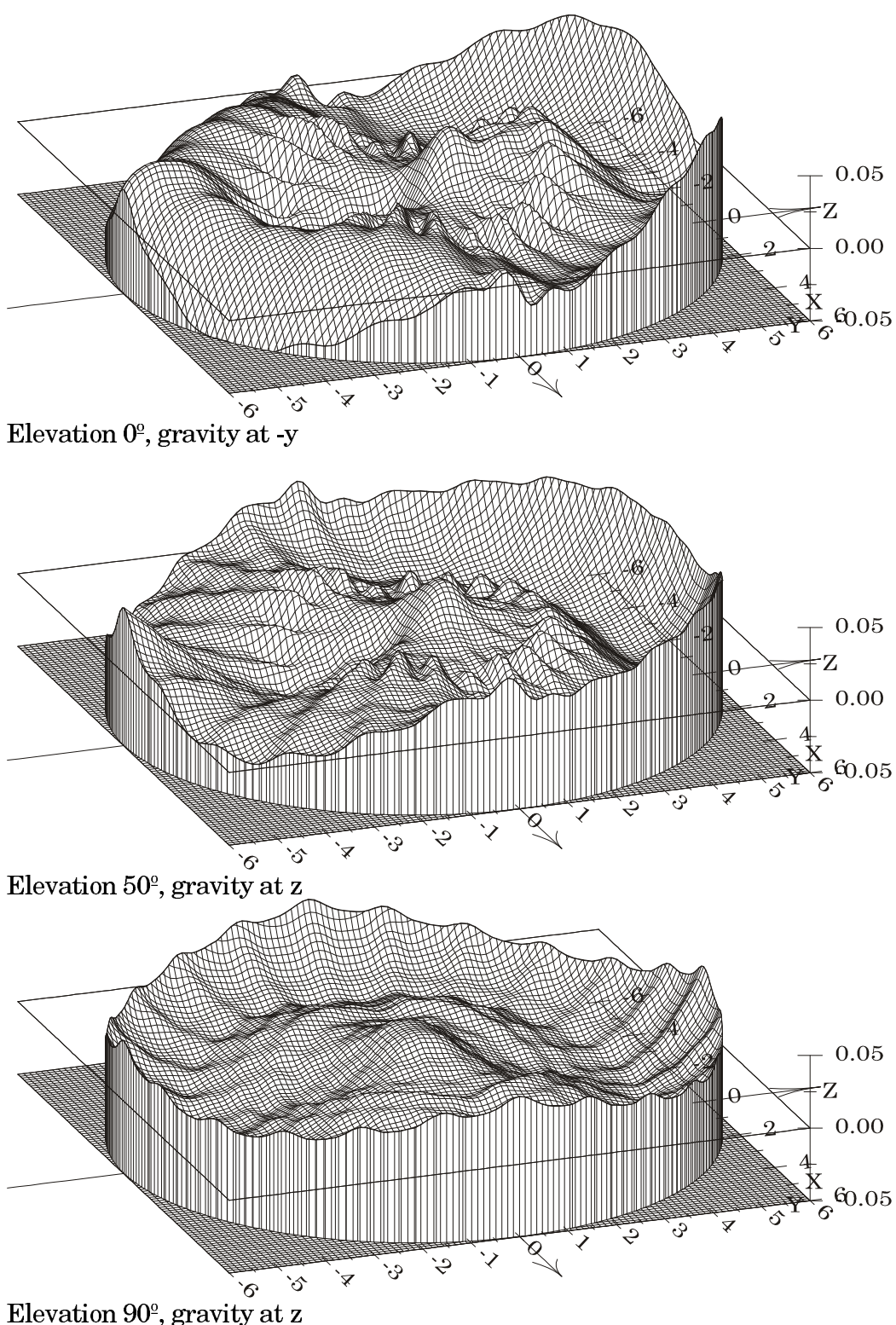


Figure 5-31 The deviation between the deformed reflector and the best fit paraboloid.

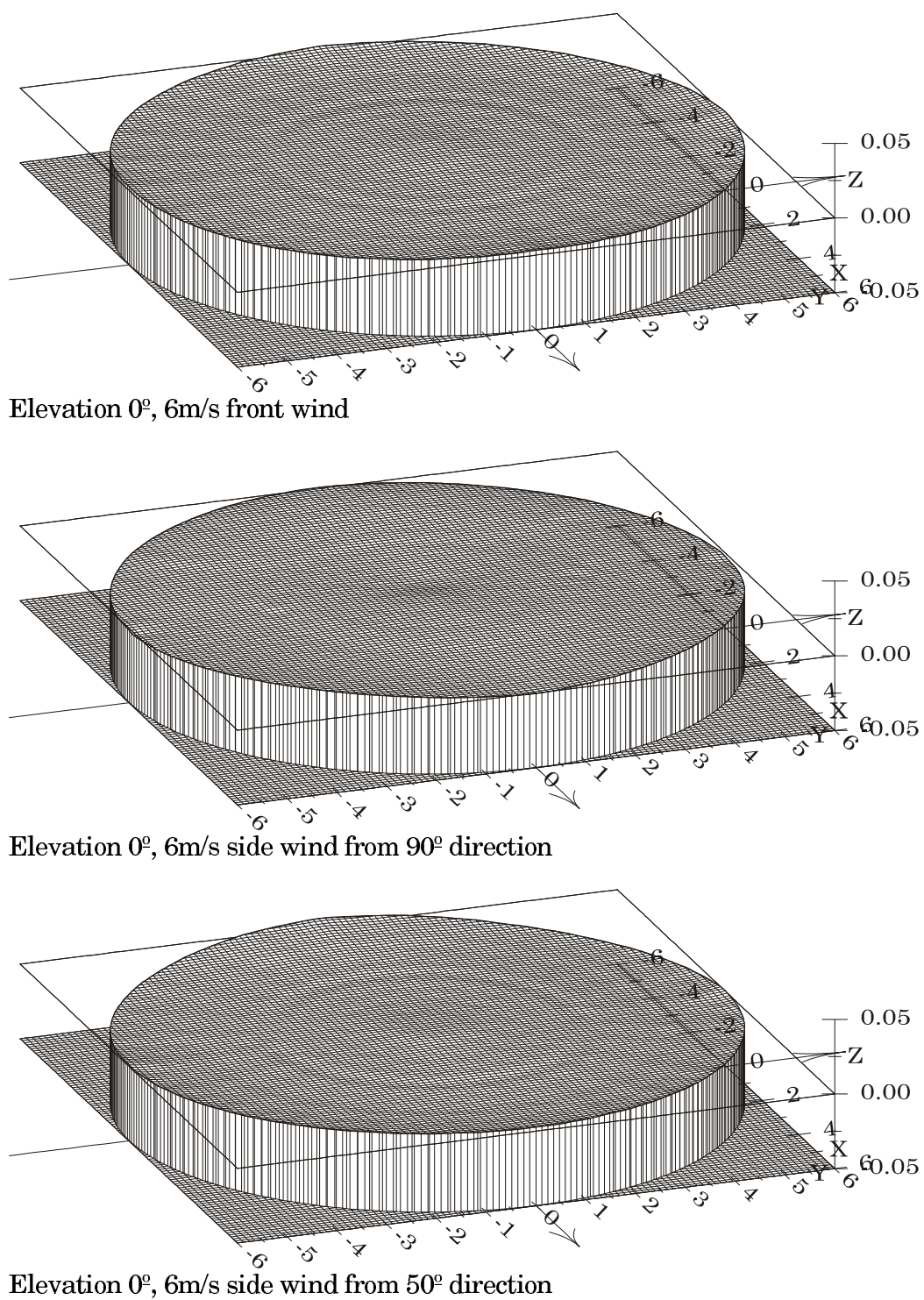
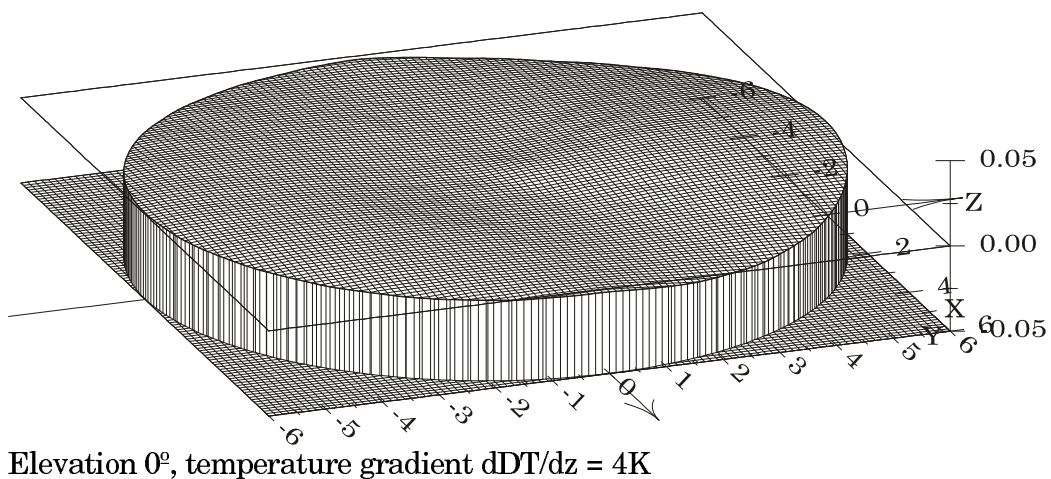
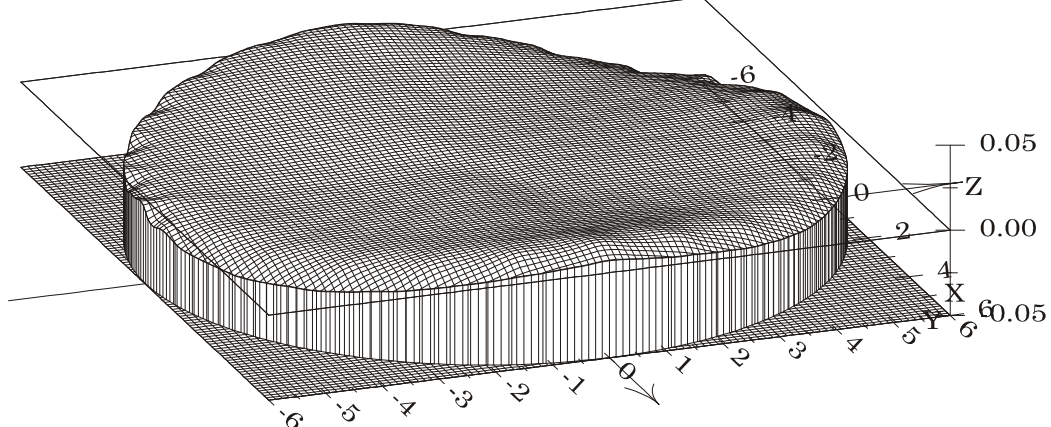


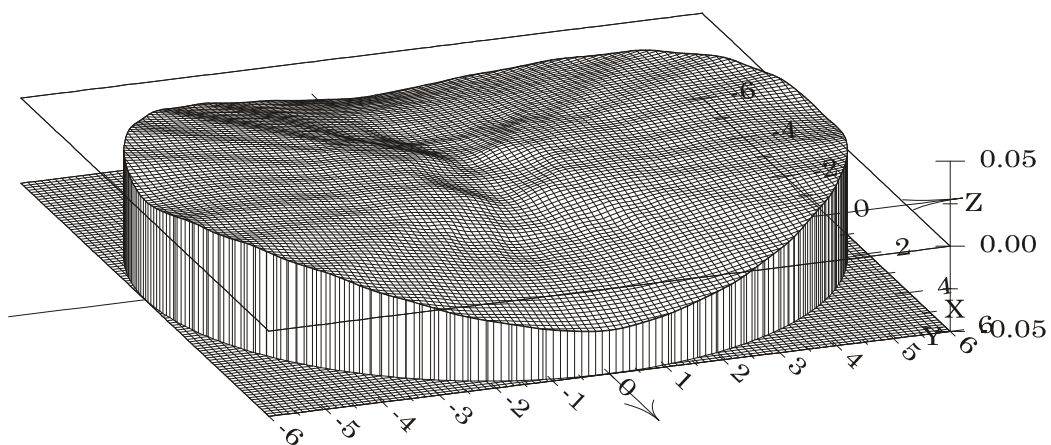
Figure 5-32 The deviation between the deformed reflector and the best fit paraboloid.



Elevation 0°, temperature gradient $dDT/dz = 4K$



Elevation 0°, temperature 2.3K from $x < 0$ to $x > 0$



Elevation 0°, absolute temperature $DT = -20K$

Figure 5-33 The deviation between the deformed reflector and the best fit paraboloid.

Surface	focal length		Vertex			Main axis rotation		Aperture
distortions	change	change	x	y	z	around x	around y	rms
	mm	df/F	mm	mm	mm	mRadians	mRadians	mm
Vertex								
elevation angle 0°								
gravity -y	0.0001	2.809E-08	0.0248	-3.7290	-0.1578	-0.4919	0.0055	0.0266
front wind	0.0398	8.299E-06	0.0000	-0.0248	-0.0113	0.0010	0.0000	0.0010
side wind 90°	-0.0054	-1.124E-06	-0.0838	0.0020	0.0031	-0.0009	0.0149	0.0014
side wind 50°	0.0356	7.425E-06	-0.0825	-0.0081	-0.0115	0.0087	0.0053	0.0018
temp gradient 2.3Kx	0.0049	1.028E-06	0.1857	-0.1744	-0.0135	0.0165	-0.0012	0.0073
temp gradient 6Ky	0.0265	5.524E-06	-0.0001	0.0672	0.3628	-0.0955	0.0000	0.0041
temp gradient 4Kz	0.0534	1.112E-05	-0.0002	0.0718	0.3633	-0.0948	0.0000	0.0042
temp -20	-0.2034	-4.238E-05	0.0005	1.8500	-0.0319	-0.0059	0.0002	0.0141
elevation angle 50°								
gravity z	0.9241	1.925E-04	0.0160	-2.4479	-0.5209	-0.3404	0.0062	0.0228
front wind	0.0356	7.410E-06	0.0000	0.0203	-0.0065	0.0076	0.0000	0.0015
side wind 90°	-0.0054	-1.124E-06	-0.0869	0.0025	0.0016	-0.0006	0.0130	0.0014
elevation angle 90°								
gravity z	1.2051	2.511E-04	0.0063	-0.1853	-0.5588	0.0271	0.0040	0.0204
front wind	-0.0055	-1.136E-06	0.0000	0.0754	0.0006	0.0148	0.0000	0.0013
side wind 90°	-0.0054	-1.124E-06	-0.0895	0.0000	0.0006	0.0000	0.0116	0.0014

Figure 5-34 The parameters for the best fit paraboloid.

5.4.2 Overview of RF calculations

The surface distortions presented in the previous sections will influence the radiated beam. The beams will be calculated for two frequencies, 243 and 720 GHz, and for two the principal polarisations of the feed.

The calculated beams will be stored on files and delivered to ESO. The table in Figure 5-35 shows all the files for surface distortion calculations. For all these calculations it is assumed that the subreflector position and tilt relative to the best fit paraboloid are unchanged compared to the un-deformed case.

Similarly, the table in Figure 5-36 shows the files for the panel distortion calculations. It should be mentioned here that, whereas the surface distortions are deterministic, the panel distortions are random with a given rms value. The panel distortions are therefore modeled by a random number generator, and in this case it is not meaningful to investigate both polarisations. Consequently, only the x-polarisation is calculated for the panel distortions. For the same reason the feed is located at the antenna focal point for all the panel distortion calculations.

File nomenclature for surface deformations	Frequency	Polarization	Manufacturer	distortion	elevation
	[GHz]	direction			[degrees]
f243_px_AEM.grd	243	x	AEM		
f243_px_AEM_grav_00.grd	243	x	AEM	gravity	0
f243_px_AEM_grav_45.grd	243	x	AEM	gravity	45
f243_px_AEM_grav_90.grd	243	x	AEM	gravity	90
f243_px_AEM_temp.grd	243	x	AEM	Uniform temp T20	
f243_py_AEM.grd	243	y	AEM		
f243_py_AEM_grav_00.grd	243	y	AEM	gravity	0
f243_py_AEM_grav_45.grd	243	y	AEM	gravity	45
f243_py_AEM_grav_90.grd	243	y	AEM	gravity	90
f243_py_AEM_temp.grd	243	y	AEM	Uniform temp T20	
f243_px_VERTEX.grd	243	x	VERTEX		
f243_px_VERTEX_grav_00.grd	243	x	VERTEX	gravity	0
f243_px_VERTEX_grav_50.grd	243	x	VERTEX	gravity	50
f243_px_VERTEX_grav_90.grd	243	x	VERTEX	gravity	90
f243_px_VERTEX_temp_00.grd	243	x	VERTEX	absolute temp dT=-20°	0
f243_px_VERTEX_wind_00.grd	243	x	VERTEX	6m/s side wind from 50°	0
f243_py_VERTEX.grd	243	y	VERTEX		
f243_py_VERTEX_grav_00.grd	243	y	VERTEX	gravity	0
f243_py_VERTEX_grav_50.grd	243	y	VERTEX	gravity	50
f243_py_VERTEX_grav_90.grd	243	y	VERTEX	gravity	90
f243_py_VERTEX_temp_00.grd	243	y	VERTEX	absolute temp dT=-20°	0
f243_py_VERTEX_wind_00.grd	243	y	VERTEX	6m/s side wind from 50°	0
f720_px_AEM.grd	720	x	AEM		
f720_px_AEM_grav_00.grd	720	x	AEM	gravity	0
f720_px_AEM_grav_45.grd	720	x	AEM	gravity	45
f720_px_AEM_grav_90.grd	720	x	AEM	gravity	90
f720_px_AEM_temp.grd	720	x	AEM	Uniform temp T20	
f720_py_AEM.grd	720	y	AEM		
f720_py_AEM_grav_00.grd	720	y	AEM	gravity	0
f720_py_AEM_grav_45.grd	720	y	AEM	gravity	45
f720_py_AEM_grav_90.grd	720	y	AEM	gravity	90
f720_py_AEM_temp.grd	720	y	AEM	Uniform temp T20	
f720_px_VERTEX.grd	720	x	VERTEX		
f720_px_VERTEX_grav_00.grd	720	x	VERTEX	gravity	0
f720_px_VERTEX_grav_50.grd	720	x	VERTEX	gravity	50
f720_px_VERTEX_grav_90.grd	720	x	VERTEX	gravity	90
f720_px_VERTEX_temp_00.grd	720	x	VERTEX	absolute temp dT=-20°	0
f720_px_VERTEX_wind_00.grd	720	x	VERTEX	6m/s side wind from 50°	0
f720_py_VERTEX.grd	720	y	VERTEX		
f720_py_VERTEX_grav_00.grd	720	y	VERTEX	gravity	0
f720_py_VERTEX_grav_50.grd	720	y	VERTEX	gravity	50
f720_py_VERTEX_grav_90.grd	720	y	VERTEX	gravity	90
f720_py_VERTEX_temp_00.grd	720	y	VERTEX	absolute temp dT=-20°	0
f720_py_VERTEX_wind_00.grd	720	y	VERTEX	6m/s side wind from 50°	0

Figure 5-35 The file names for the different surface deformation calculations.

File nomenclature for panel deformations	Frequency	Polarization	Manufacturer	distortion
	[GHz]	direction		
f243_px_AEM_panel.grd	243	x	AEM	none
f243_px_AEM_panel_mount.grd	243	x	AEM	mounting inaccuracies
f243_px_AEM_panel_manufact.grd	243	x	AEM	manufacturing errors
f243_px_VERTEXE_panel.grd	243	x	VERTEXE	none
f243_px_VERTEXE_panel_mount.grd	243	x	VERTEXE	mounting inaccuracies
f243_px_VERTEXE_panel_manufact.grd	243	x	VERTEXE	manufacturing errors
f720_px_AEM_panel.grd	720	x	AEM	none
f720_px_AEM_panel_mount.grd	720	x	AEM	mounting inaccuracies
f720_px_AEM_panel_manufact.grd	720	x	AEM	manufacturing errors
f720_px_VERTEXE_panel.grd	720	x	VERTEXE	none
f720_px_VERTEXE_panel_mount.grd	720	x	VERTEXE	mounting inaccuracies
f720_px_VERTEXE_panel_manufact.grd	720	x	VERTEXE	manufacturing errors

Figure 5-36 The file names for the different panel distortion calculations.

5.4.3 RF calculations for the AEM antenna

5.4.3.1 Surface deformations

This section contains the results for the surface deformations and they are summarised in the tables in Figure 5-37 and 5-38 for the frequencies 243 and 720 GHz, respectively. The tables give the results both for the nominal antenna with and without struts as well as for the selected deformation cases with struts. The tables show the direction of the beam maximum, the change in direction due to deformation and the beam peak level in dBi. The column shows the rms error calculated from the peak gain decrease.

In order to illustrate the influence of the surface deformations Figures 5-39 to 5-46 show, as an example, the contour plots and three pattern cuts both for the nominal antenna and for gravitation deformation at 0° elevation and at both frequencies. It is clearly seen that the surface deformations are much more critical at the highest frequency.

AEM struts	Beam direction		direction change		Beam peak difference		Aperture distortion
	mRadians		mRadians		Co	Co	
	u	v	du	dv	dBi	dB	mm
243 GHz							
x-pol							
no struts	-0.8513	-0.8513			88.90		
nominal	-0.8513	-0.8513			88.71		
gravity_00	-0.8680	-0.6628	-0.0168	0.1885	88.65	-0.06	0.023
gravity_45	-0.8637	-0.7289	-0.0124	0.1224	88.68	-0.03	0.016
gravity_90	-0.8510	-0.8762	0.0003	-0.0250	88.70	-0.01	0.009
uniform temperature T20	-0.8520	-0.8443	-0.0007	0.0070	88.69	-0.02	0.013
y-pol							
no struts	-0.8513	-0.8513			88.90		
nominal	-0.8513	-0.8513			88.71		
gravity_00	-0.8680	-0.6628	-0.0168	0.1885	88.65	-0.06	0.023
gravity_45	-0.8637	-0.7289	-0.0124	0.1224	88.68	-0.03	0.016
gravity_90	-0.8510	-0.8762	0.0003	-0.0250	88.70	-0.01	0.009
uniform temperature T20	-0.8520	-0.8443	-0.0007	0.0070	88.69	-0.02	0.013

Figure 5-37 Table showing the results at 243 GHz for the AEM antenna.

AEM struts	Beam direction		direction change		Beam peak difference		Aperture distortion
	mRadians		mRadians		Co	Co	
	u	v	du	dv	dB	dB	mm
720 GHz							
x-pol							
no struts	0.0000	-0.4808			98.21		
nominal	0.0000	-0.4808			98.01		
gravity_00	-0.0167	-0.2923	-0.0167	0.1885	97.51	-0.50	0.0225
gravity_45	-0.0124	-0.3584	-0.0124	0.1224	97.65	-0.36	0.0191
gravity_90	-0.0002	-0.5057	-0.0002	-0.0249	97.81	-0.20	0.0142
uniform temperature T20	-0.0014	-0.4739	-0.0014	0.0069	97.82	-0.19	0.0139
y-pol							
no struts	0.0000	-0.4808			98.20		
nominal	0.0000	-0.4808			98.01		
gravity_00	-0.0167	-0.2923	-0.0167	0.1885	97.50	-0.51	0.0227
gravity_45	-0.0124	-0.3584	-0.0124	0.1224	97.64	-0.37	0.0194
gravity_90	-0.0002	-0.5057	-0.0002	-0.0250	97.80	-0.21	0.0146
uniform temperature T20	-0.0013	-0.4740	-0.0013	0.0068	97.81	-0.20	0.0142

Figure 5-38 Table showing the results at 720 GHz for the AEM antenna.

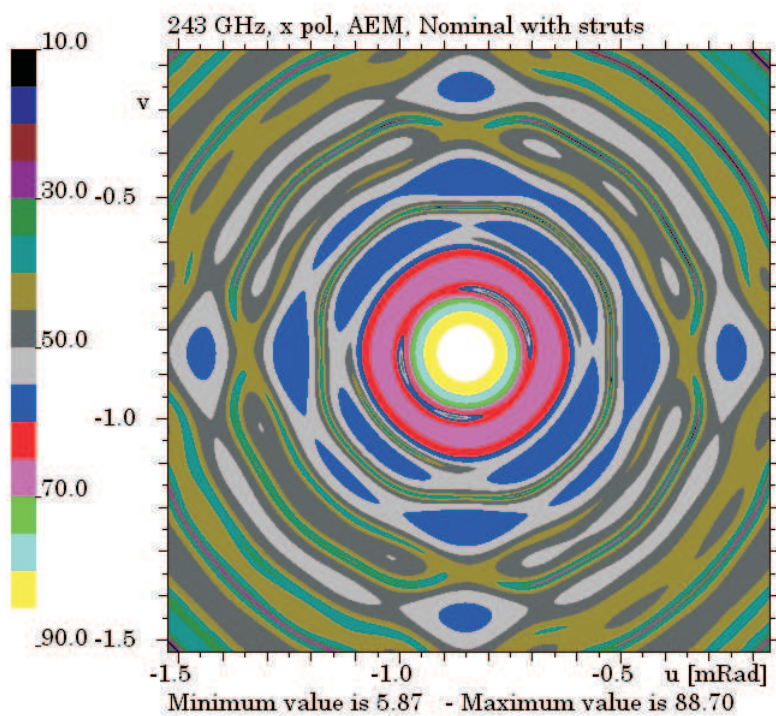


Figure 5-39 Contour plot of the nominal beam at 243 GHz for the AEM antenna with struts.

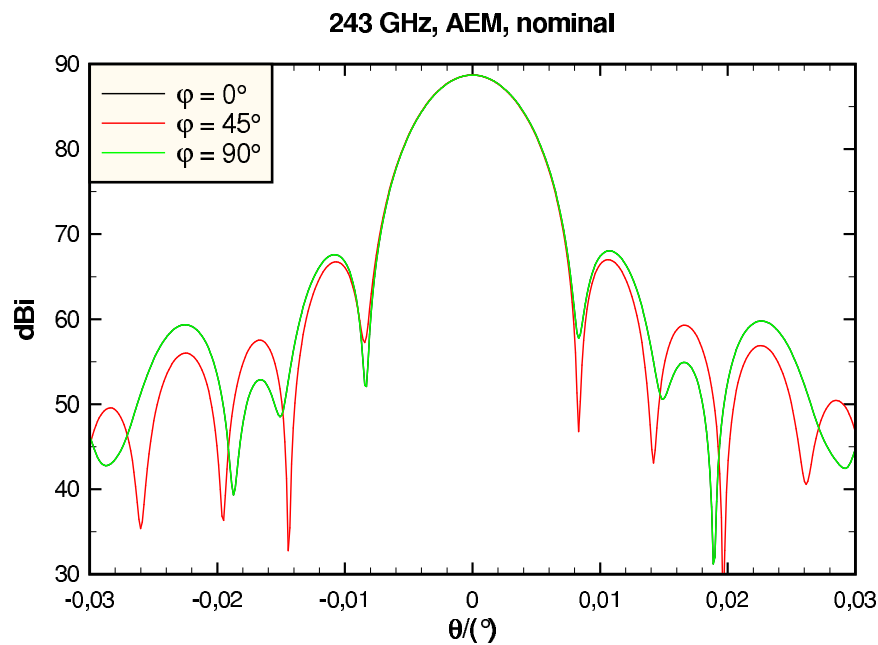


Figure 5-40 Pattern cuts through the maximum of the nominal beam at 243 GHz for the AEM antenna with struts.

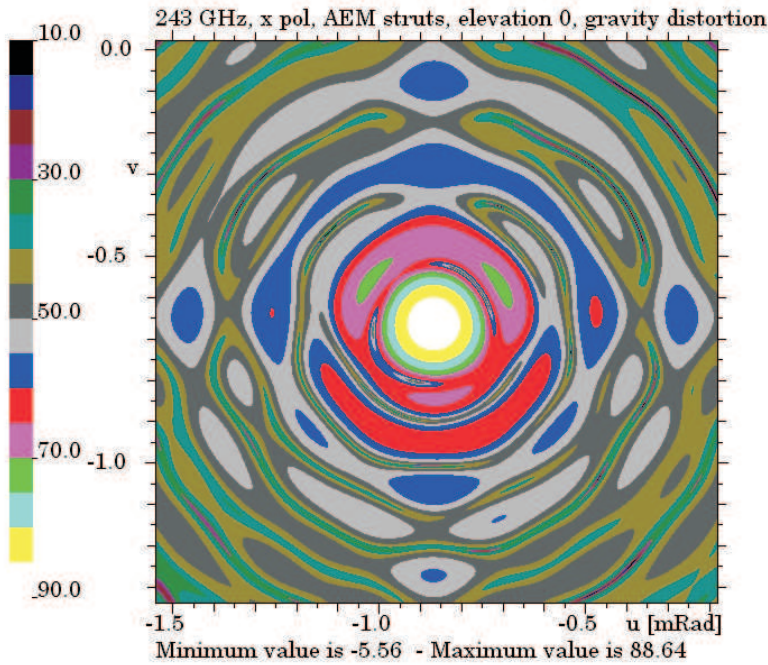


Figure 5-41 Contour plot of the beam at 243 GHz for the AEM antenna with struts. Surface deformation: gravitation at 0° elevation

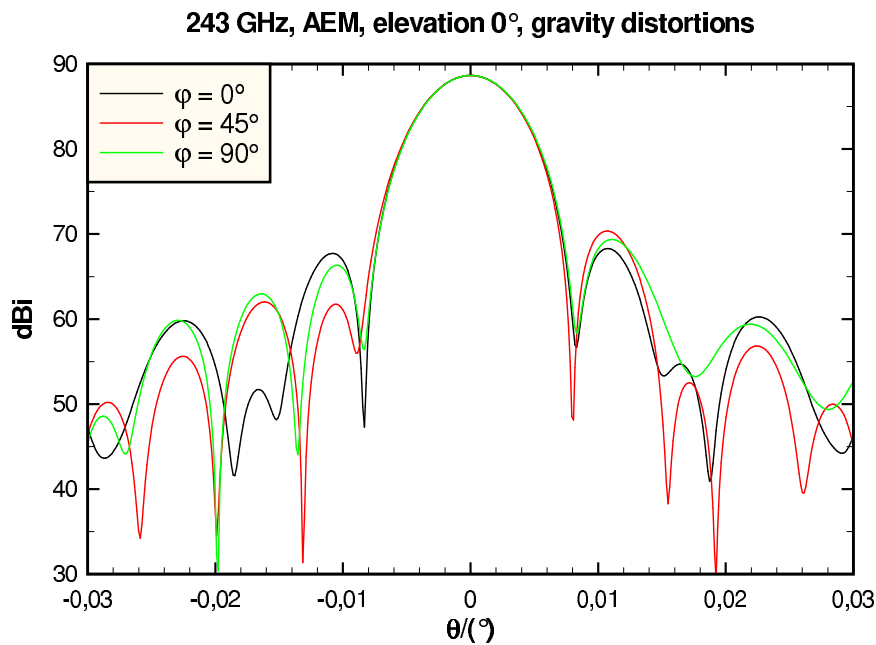


Figure 5-42 Pattern cuts through the maximum of the beam at 243 GHz for the AEM antenna with struts. Surface deformation: gravitation at 0° elevation

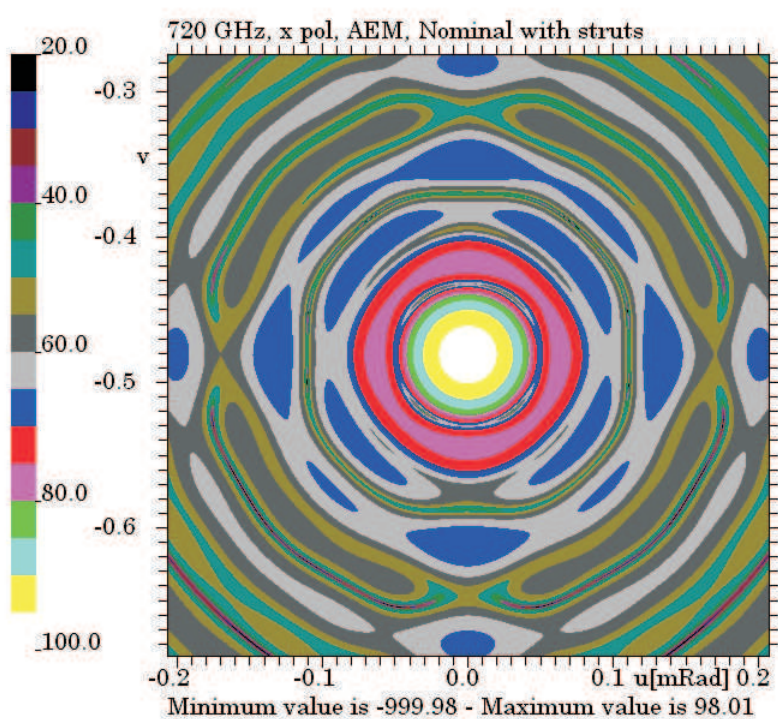


Figure 5-43 Contour plot of the nominal beam at 720 GHz for the AEM antenna with struts.

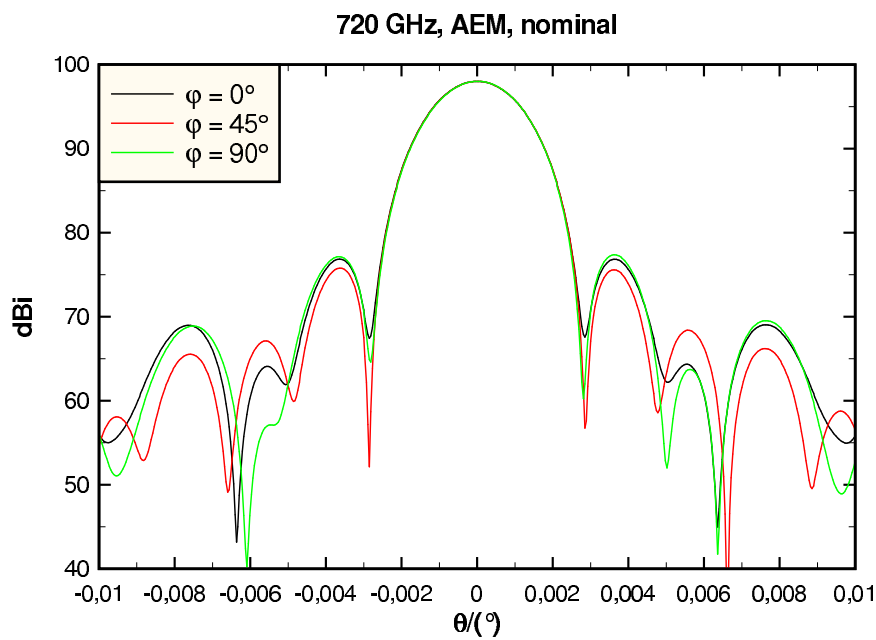


Figure 5-44 Pattern cuts through the maximum of the nominal beam at 720 GHz for the AEM antenna with struts.

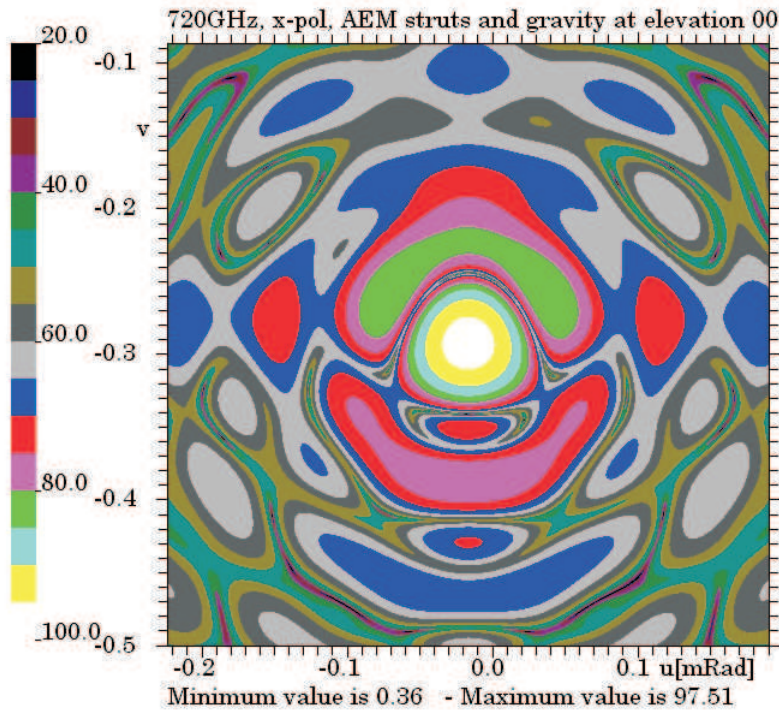


Figure 5-45 Contour plot of the beam at 720 GHz for the AEM antenna with struts. Surface deformation: gravitation at 0° elevation

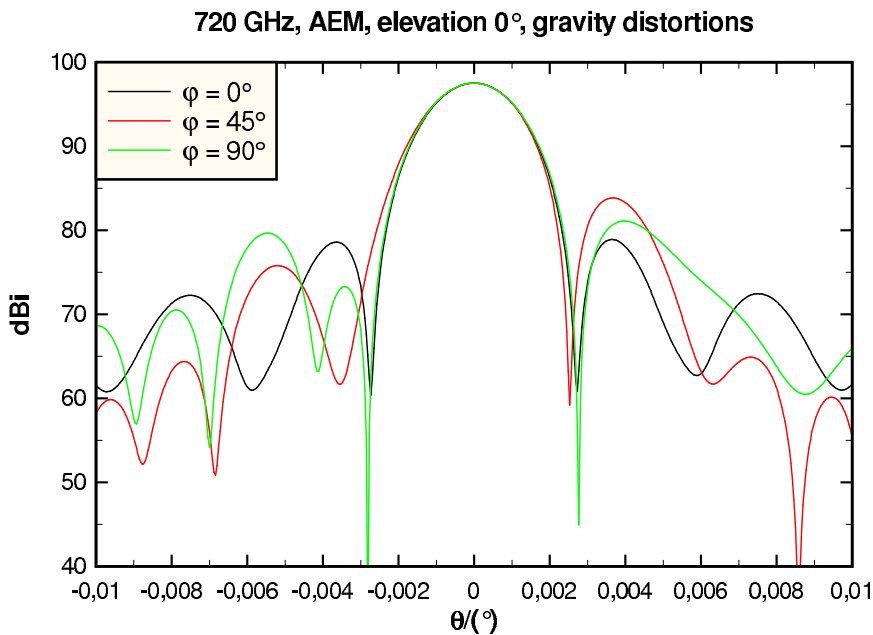


Figure 5-46 Pattern cuts through the maximum of the beam at 720 GHz for the AEM antenna with struts. Surface deformation: gravitation at 0° elevation

5.4.3.2 Panel alignment and deformations

The influence of the panel gaps was investigated in Section 2.4, and it was found that this effect is very small when the surface shape and alignment of the panels is ideal.

In this section both panel deformation and panel alignment will be investigated. The table in Figure 5-47 is from the document "ANTD-3300000-3-049-REP.pdf" and it shows the different contributions to the total surface errors. The table is divided in four groups where the first is related to the shape of the panels and the third is related to the mounting accuracy of the panels.

Based on the numbers in this table it was decided to model the panel shape error as a smooth random distortion all over the reflector with an rms error of $8 \mu\text{m}$ and a correlation distance approximately equal to the panel size, in this case 1.09 m. The shape of these distortions are illustrated in Figure 5-48.

PANELS'	DAY	NIGHT	DAY	NIGHT
	STEADY	GUST	IN MICRONS	IN MICRONS
MANUFACTURING	4.5	4.5	4.5	4.5
AGING	2.0	2.0	2.0	2.0
GRAVITY	5.3	5.3	5.3	5.3
WIND	0.8	1.9	0.9	2.1
ABSOLUTE TEMPERATURE	0.8	1.6	0.8	1.6
TEMPERATURE GRADIENT	3.8	0.0	3.8	0.0
TOTAL PANEL RSS	8.2	7.6	8.3	7.7
BACKUP STRUCTURE'				
GRAVITY (IDEAL)	8.8	8.8	8.8	8.8
GRAVITY (Departure from ideal)	2.0	2.0	2.0	2.0
WIND	0.9	2.1	1.1	2.3
ABSOLUTE TEMPERATURE	7.0	7.0	7.0	7.0
TEMPERATURE GRADIENT	0.7	0.0	0.7	0.0
AGING and MOISTURE	2.0	2.0	2.0	2.0
TOTAL BACKUP RSS	11.7	11.8	11.7	11.8
PANEL MOUNTING'				
ABSOLUTE TEMPERATURE	2.0	2.0	2.0	2.0
TEMPERATURE GRADIENT	2.0	0.0	2.0	0.0
PANEL LOCATION IN PLANE	3.0	3.0	3.0	3.0
PANEL ADJUSTMENT PERP. TO PLANE'	2.0	2.0	2.0	2.0
GRAVITY	0.0	0.0	0.0	0.0
WIND	0.0	0.0	0.0	0.0
TOTAL MOUNTING RSS	4.6	4.1	4.6	4.1
SECONDARY MIRROR				
MANUFACTURING	5.8	5.8	5.8	5.8
GRAVITY	0.1	0.1	0.1	0.1
WIND	0.1	0.1	0.1	0.1
ABSOLUTE TEMPERATURE	1.0	1.0	1.0	1.0
TEMPERATURE GRADIENT	0.1	0.0	0.1	0.0
AGING	2.0	2.0	2.0	2.0
ALIGNMENT (coma error)	1.7	1.7	1.7	1.7
TOTAL SECONDARY MIRROR RSS	6.5	6.5	6.5	6.5
TOTAL ERROR EXCLUDING SURFACE ALIGNMENT	16.3	16.0	16.3	16.1
SURFACE ALIGNMENT ERROR (HOLOGRAPHY)	10.0	10.0	10.0	10.0
UNANTICATED ERRORS	2.0	2.0	2.0	2.0
TOTAL SURFACE ACCURACY ERROR	19.3	19.0	19.3	19.0

Figure 5-47 Table showing the various sources of reflector surface errors

Each panel is attached at five attachment points and the accuracy at these points is assumed to be $5 \mu\text{m}$. A random number generator is used to model the attachment point positions. The mounting errors are modeled by tilting each panel individually, without changing its shape, such that it passes through the five points in the best possible way. The principle is illustrated in Figure 5-49 where the errors are increased by a factor 10000.

The calculation of the influence of the panel errors including the

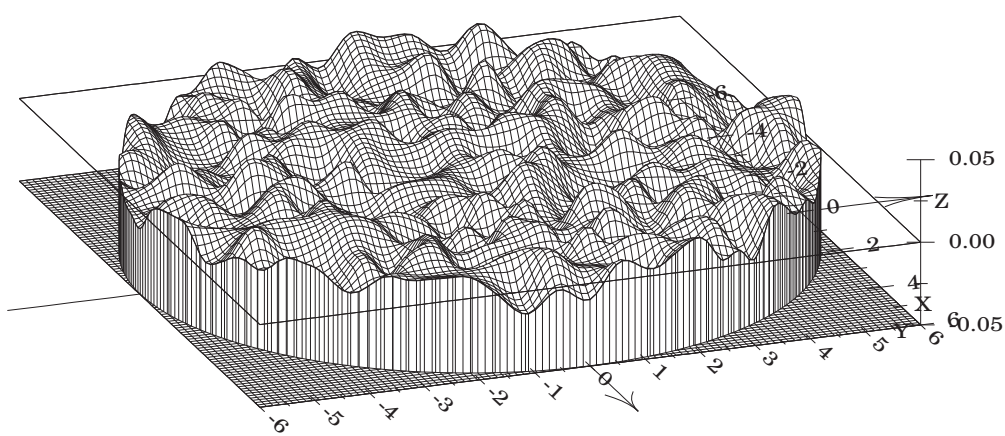


Figure 5-48 Surface shape illustrating the panel manufacturing errors

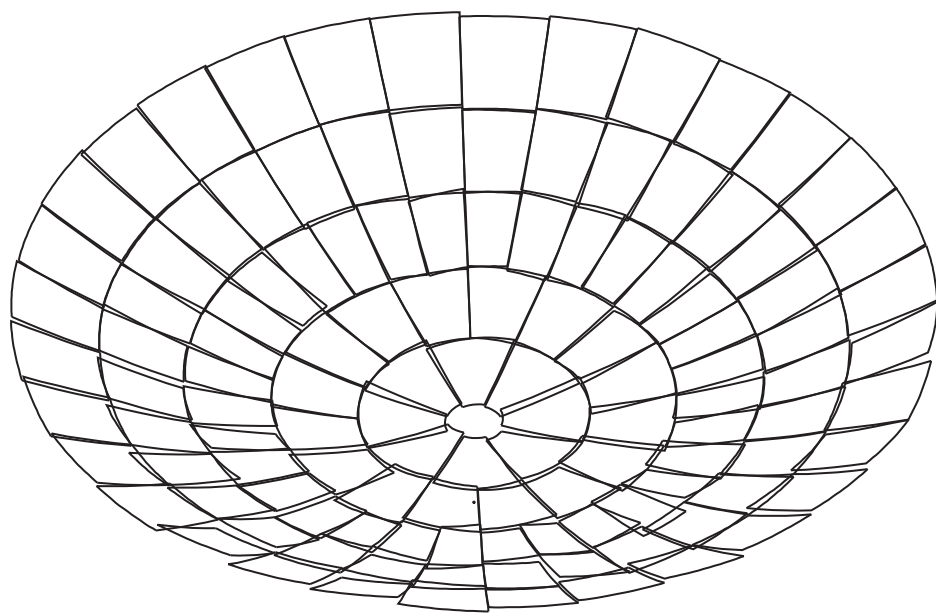


Figure 5-49 Main reflector illustrating the panel alignment errors. The realistic errors are multiplied 10,000 in this figure

struts is very complicated and time consuming. Since the impact from the panel errors is small it is calculated for the antenna without struts and then the panel error field is added to the nominal pattern with struts.

The following Figures 5-50 to 5-57 show contour plots and pattern cuts for the two types of panel errors separately: the manufacturing errors affecting the shape of the panels and the alignment errors affecting the orientation of the panels. The pattern cuts show the nominal pattern without panel errors in black, the pattern with errors in red and the difference field in green.

The reduction in gain at 243 GHz due to the panel errors is 0.02 dB and 0.00 dB for manufacturing and alignment errors, respectively. The corresponding numbers at 720 GHz are 0.18 and 0.03 dB.

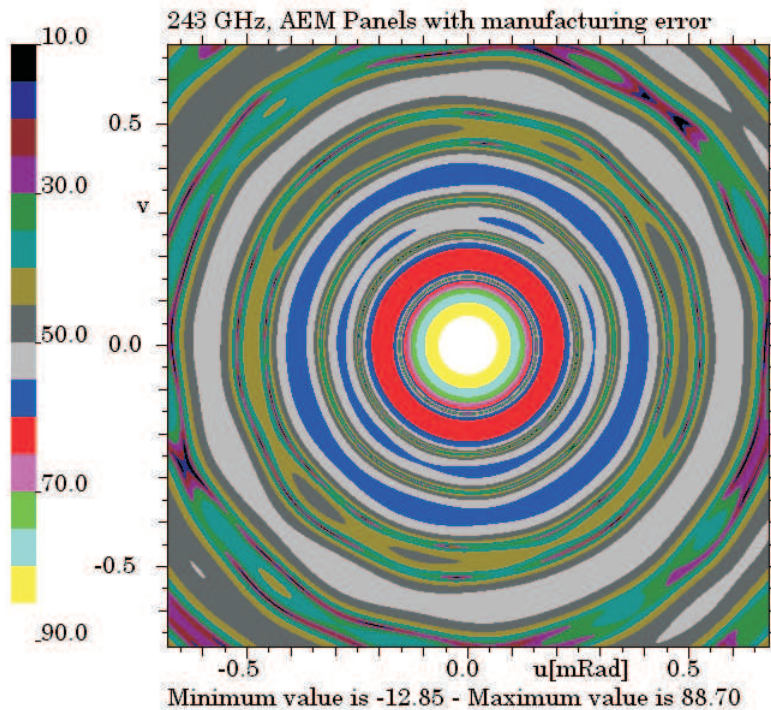


Figure 5-50 Contour plot of the beam at 243 GHz for the AEM antenna with panel manufacturing errors

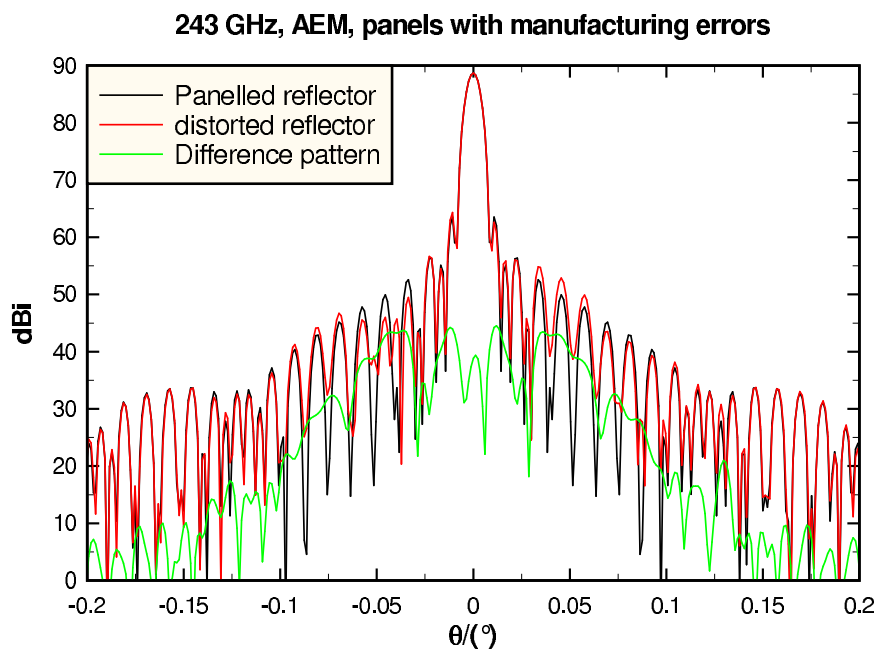


Figure 5-51 Pattern cuts at 243 GHz for the AEM antenna with panel manufacturing errors

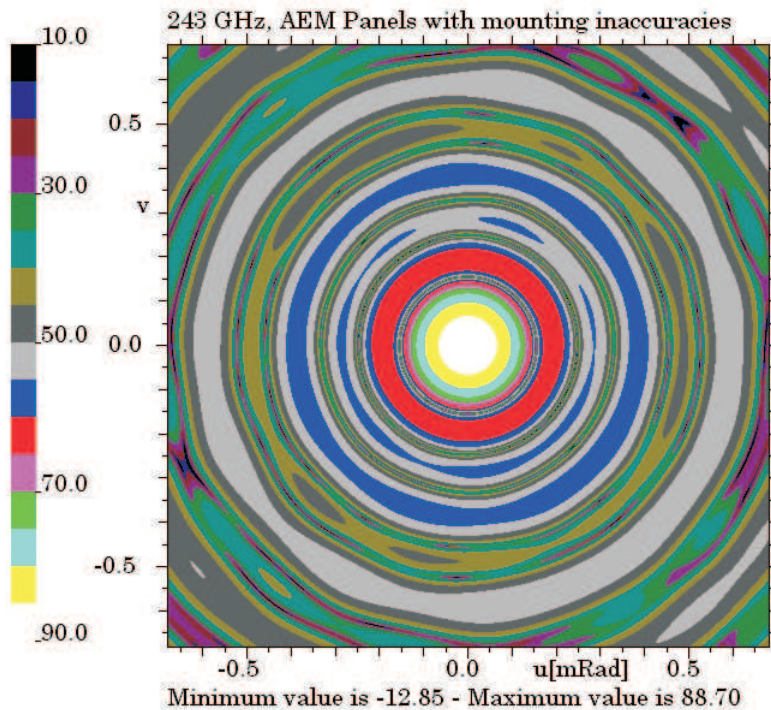


Figure 5-52 Contour plot of the beam at 243 GHz for the AEM antenna with panel alignment errors

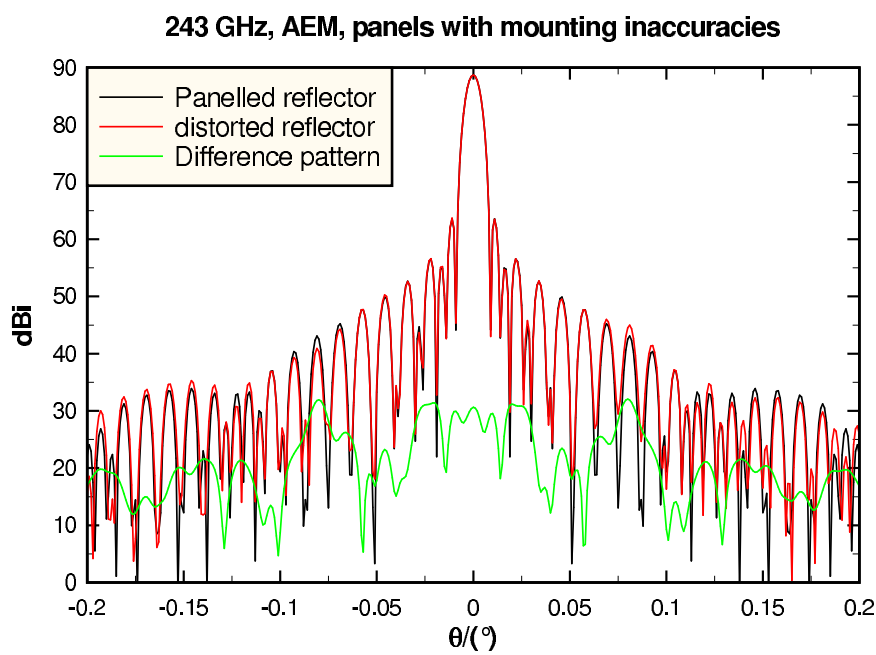


Figure 5-53 Pattern cuts at 243 GHz for the AEM antenna with panel alignment errors

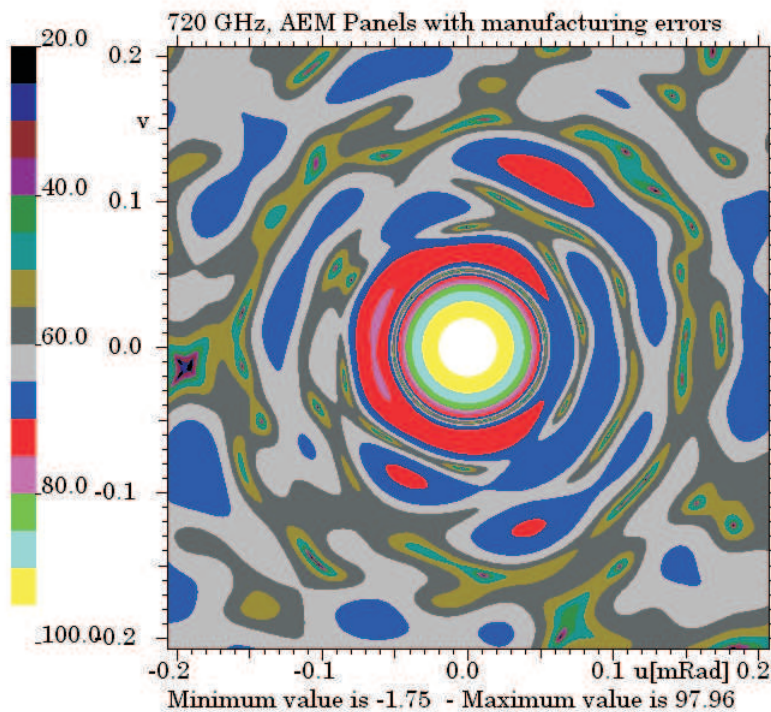


Figure 5-54 Contour plot of the beam at 720 GHz for the AEM antenna with panel manufacturing errors

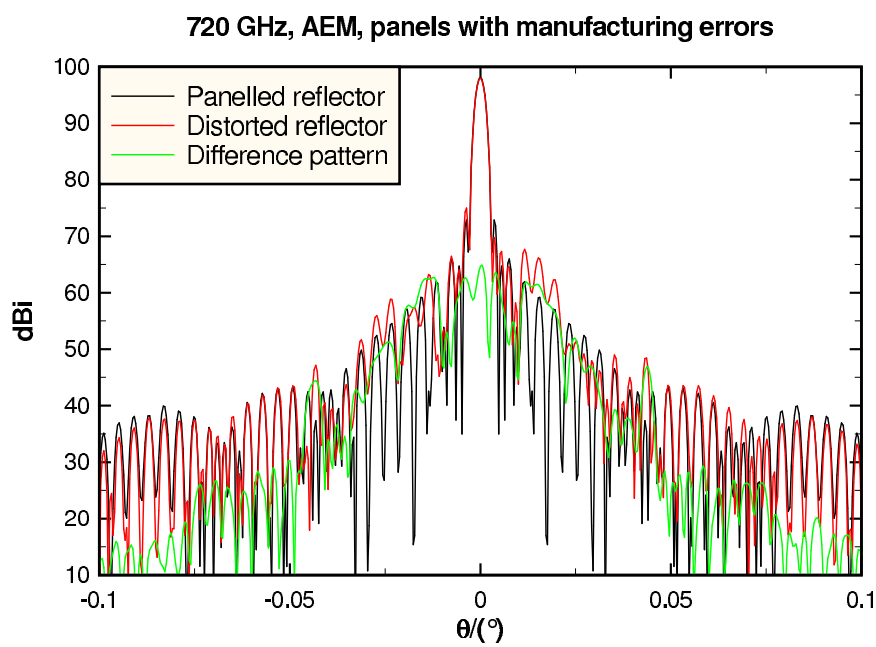


Figure 5-55 Pattern cuts at 720 GHz for the AEM antenna with panel manufacturing errors

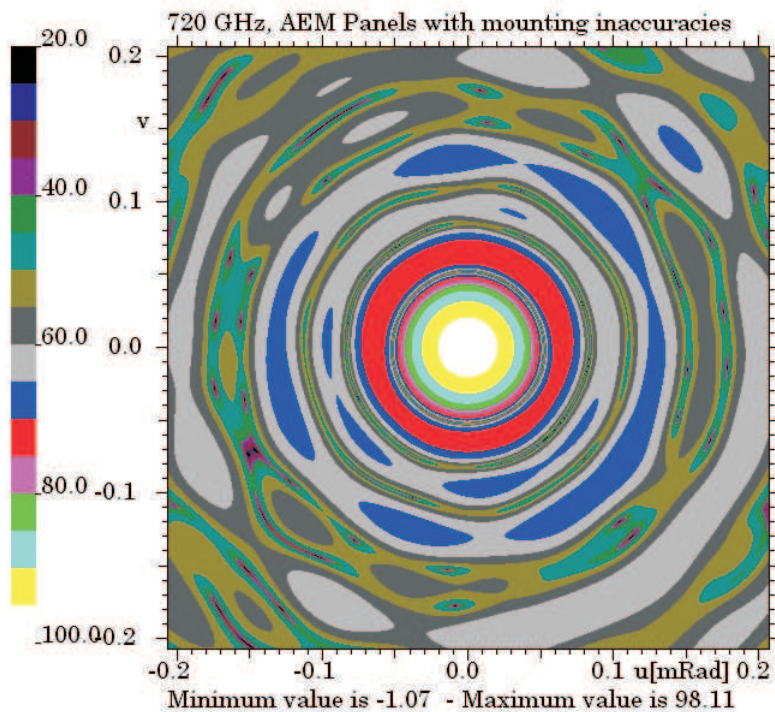


Figure 5-56 Contour plot of the beam at 720 GHz for the AEM antenna with panel alignment errors

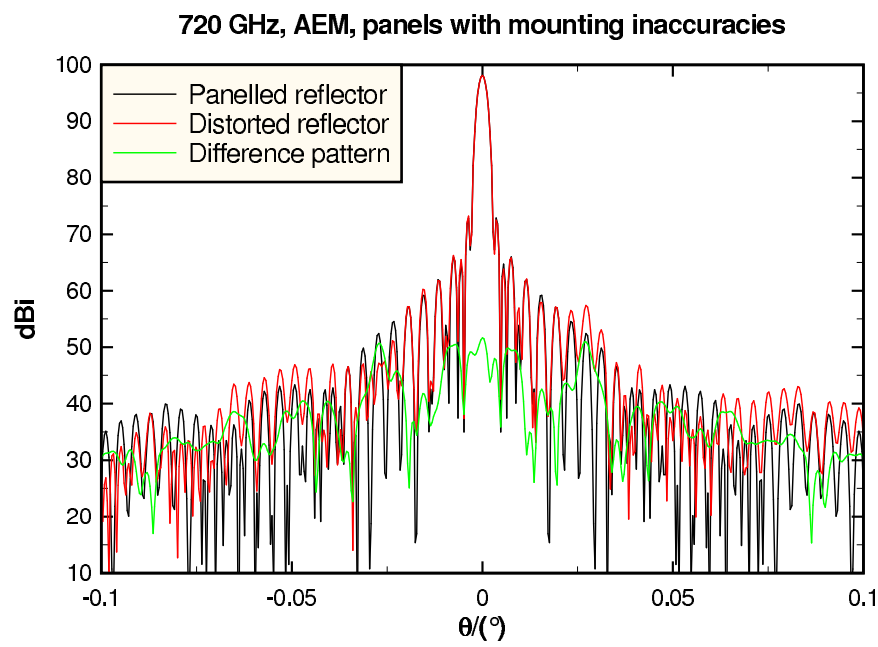


Figure 5-57 Pattern cuts at 720 GHz for the AEM antenna with panel alignment errors

5.4.4 RF calculations for the Vertex antenna

5.4.4.1 Surface deformations

This section contains the results for the surface deformations and they are summarised in the tables in Figure 5-58 and 5-59 for the frequencies 243 and 720 GHz, respectively. The tables give the results both for the nominal antenna with and without struts as well as for the selected deformation cases with struts. The tables show the direction of the beam maximum, the change in direction due to deformation and the beam peak level in dBi. The column shows the rms error calculated from the peak gain decrease.

In order to illustrate the influence of the surface deformations Figures 5-60 to 5-67 show, as an example, the contour plots and three pattern cuts both for the nominal antenna and for gravitation deformation at 0° elevation and at both frequencies. It is clearly seen that the surface deformations are much more critical at the highest frequency.

VERTEX struts	Beam direction		direction change		Beam peak	difference	Aperture distortion
	mRadians		mRadians		Co	Co	delta rms
	u	v	du	dv	dBi	dB	mm
243 GHz							
x-pol							
no struts	-0.8513	-0.8513			88.90		
nominal	-0.8513	-0.8513			88.75		
gravity_00	-0.8456	-0.4050	0.0056	0.4463	88.67	-0.08	0.027
gravity_50	-0.8447	-0.5408	0.0066	0.3104	88.69	-0.06	0.023
gravity_90	-0.8468	-0.8795	0.0045	-0.0282	88.70	-0.05	0.021
absolute temperature dT=20K	-0.8513	-0.8263	-0.0001	0.0250	88.73	-0.02	0.013
elevation 0, 50 deg side wind 6m/s	-0.8463	-0.8549	0.0050	-0.0037	88.75	0.00	0.000
y-pol							
no struts	-0.8513	-0.8513			88.90		
nominal	-0.8512	-0.8513			88.75		
gravity_00	-0.8457	-0.4050	0.0056	0.4463	88.67	-0.08	0.027
gravity_50	-0.8447	-0.5408	0.0066	0.3104	88.69	-0.06	0.023
gravity_90	-0.8468	-0.8795	0.0045	-0.0282	88.70	-0.05	0.021
absolute temperature dT=20K	-0.8513	-0.8263	-0.0001	0.0250	88.73	-0.02	0.013
elevation 0, 50 deg side wind 6m/s	-0.8463	-0.8549	0.0050	-0.0037	88.75	0.00	0.000

Figure 5-58 Table showing the results at 243 GHz for the Vertex antenna.

VERTEX struts	Beam direction		direction change		Beam peak	difference	Aperture distortion
	mRadians		mRadians		Co	Co	delta rms
	u	v	du	dv	dBi	dB	mm
720 GHz							
x-pol							
no struts	0.0000	-0.4808			98.21		
nominal	0.0000	-0.4808			98.05		
gravity_00	0.0057	-0.0345	0.0057	0.4463	97.36	-0.69	0.0264
gravity_50	0.0063	-0.1704	0.0063	0.3104	97.46	-0.59	0.0244
gravity_90	0.0040	-0.5091	0.0040	-0.0283	97.55	-0.50	0.0225
absolute temperature dT=20K	0.0002	-0.4559	0.0002	0.0248	97.97	-0.08	0.0090
elevation 0, 50 deg side wind 6m/s	0.0049	-0.4845	0.0049	-0.0037	98.04	-0.01	0.0032
y-pol							
no struts	0.0000	-0.4808			98.21		
nominal	0.0000	-0.4808			98.06		
gravity_00	0.0057	-0.0345	0.0057	0.4463	97.35	-0.71	0.0268
gravity_50	0.0064	-0.1705	0.0064	0.3103	97.45	-0.61	0.0249
gravity_90	0.0041	-0.5092	0.0041	-0.0284	97.54	-0.52	0.0229
absolute temperature dT=20K	0.0002	-0.4560	0.0002	0.0248	97.96	-0.10	0.0101
elevation 0, 50 deg side wind 6m/s	0.0050	-0.4845	0.0050	-0.0037	98.03	-0.03	0.0055

Figure 5-59 Table showing the results at 720 GHz for the Vertex antenna.

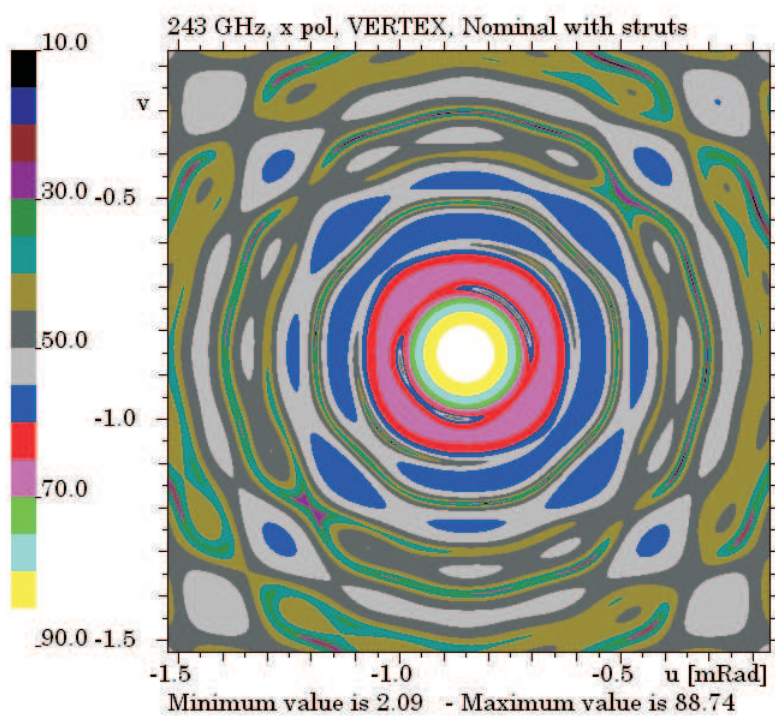


Figure 5-60 Contour plot of the nominal beam at 243 GHz for the Vertex antenna with struts.

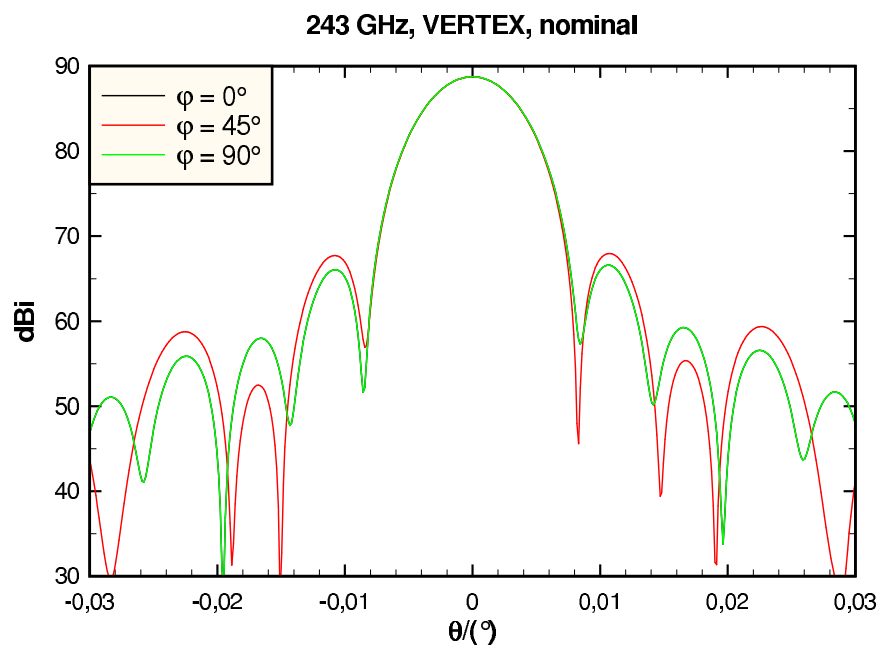


Figure 5-61 Pattern cuts through the maximum of the nominal beam at 243 GHz for the Vertex antenna with struts.

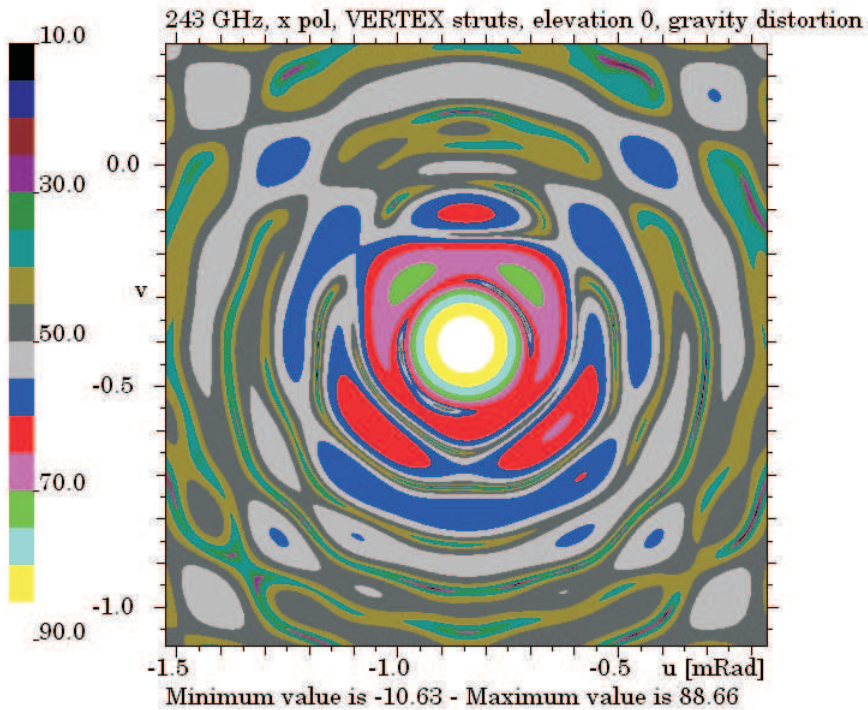


Figure 5-62 Contour plot of the beam at 243 GHz for the Vertex antenna with struts. Surface deformation: gravitation at 0° elevation

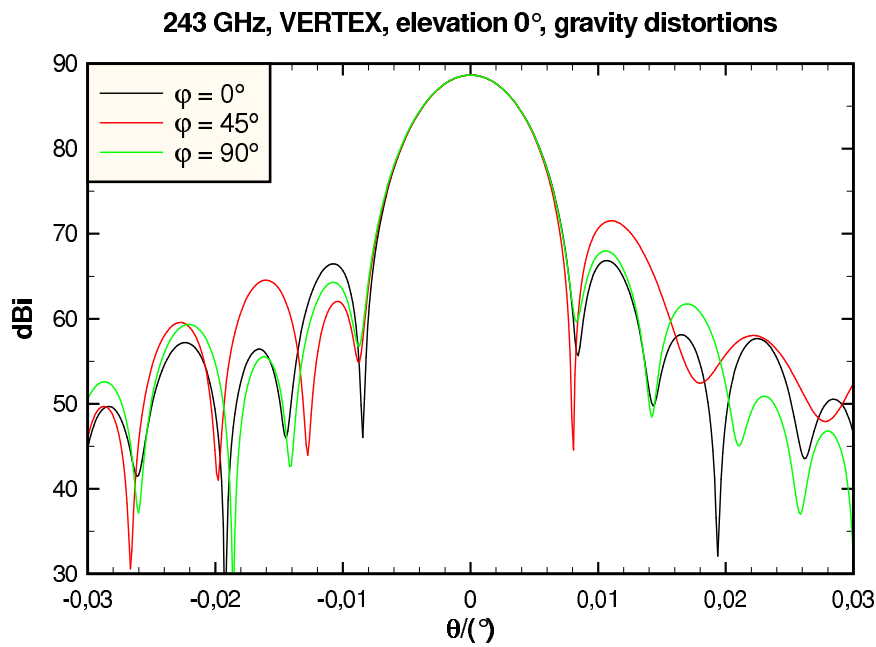


Figure 5-63 Pattern cuts through the maximum of the beam at 243 GHz for the Vertex antenna with struts. Surface deformation: gravitation at 0° elevation

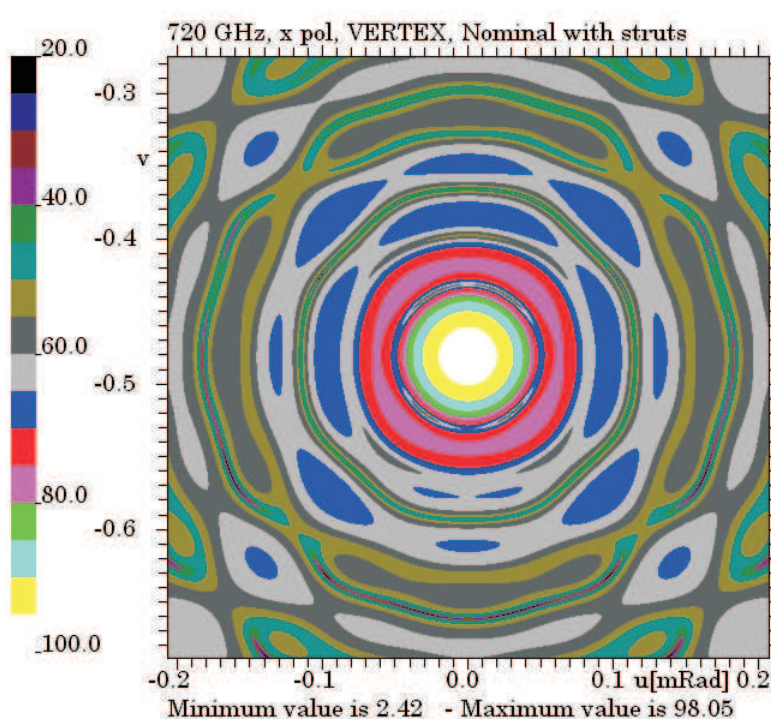


Figure 5-64 Contour plot of the nominal beam at 720 GHz for the Vertex antenna with struts.

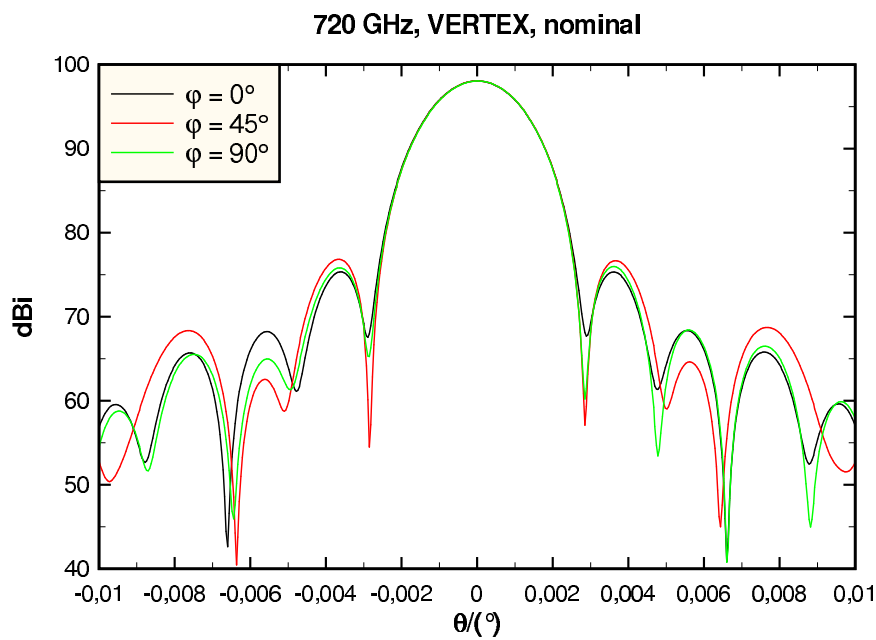


Figure 5-65 Pattern cuts through the maximum of the nominal beam at 720 GHz for the Vertex antenna with struts.

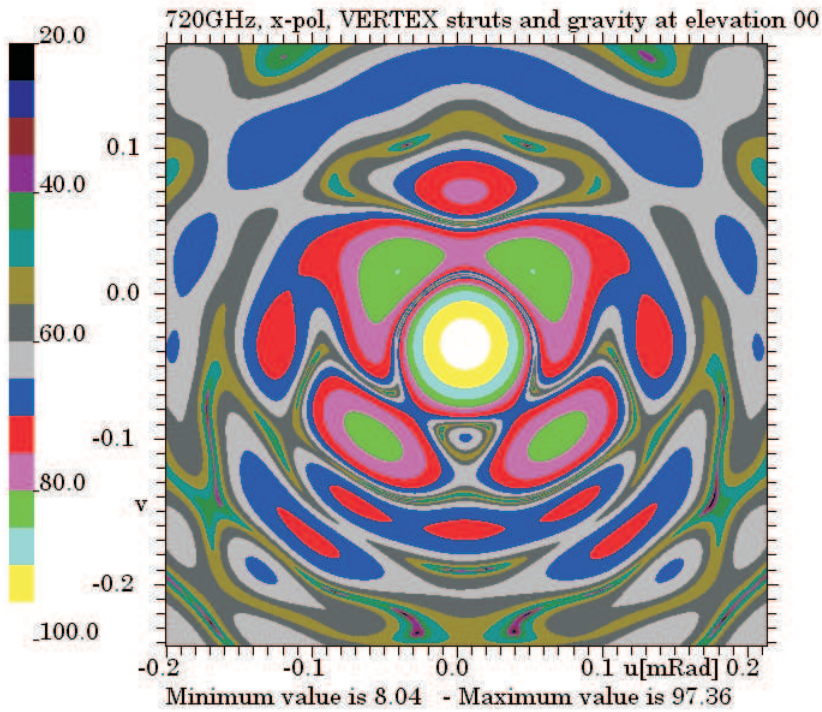


Figure 5-66 Contour plot of the beam at 720 GHz for the Vertex antenna with struts. Surface deformation: gravitation at 0° elevation

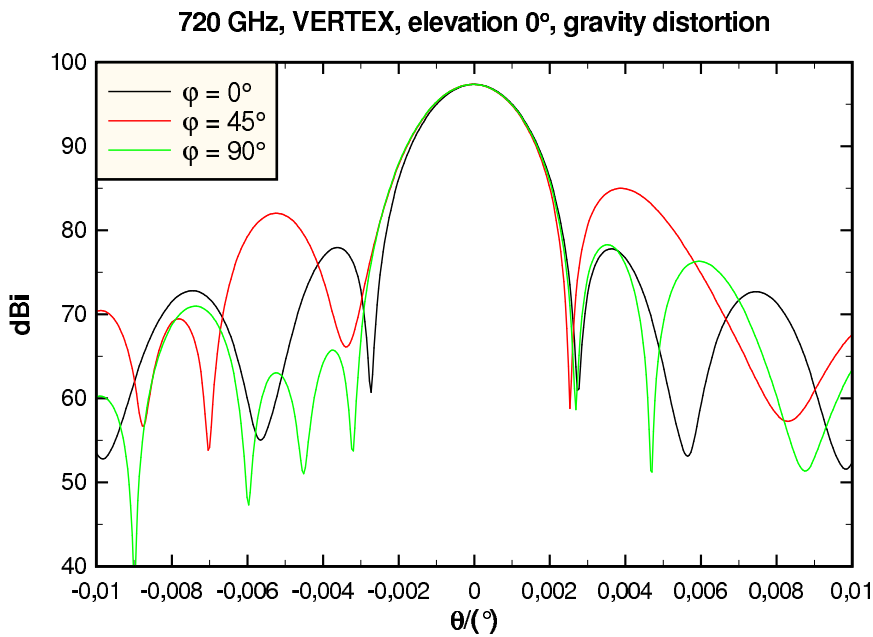


Figure 5-67 Pattern cuts through the maximum of the beam at 720 GHz for the Vertex antenna with struts. Surface deformation: gravitation at 0° elevation

5.4.4.2 Panel alignment and deformations

The details about the panel errors for the Vertex antenna design have not been provided to TICRA. In the following it is therefore assumed that the errors are the same as for the AEM antenna. The panel shape error will be modeled as a smooth random distortion all over the reflector with an rms error of $8 \mu\text{m}$ and a correlation distance approximately equal to the panel size, in this case 0.57 m. The shape of these distortions are illustrated in Figure 5-68.

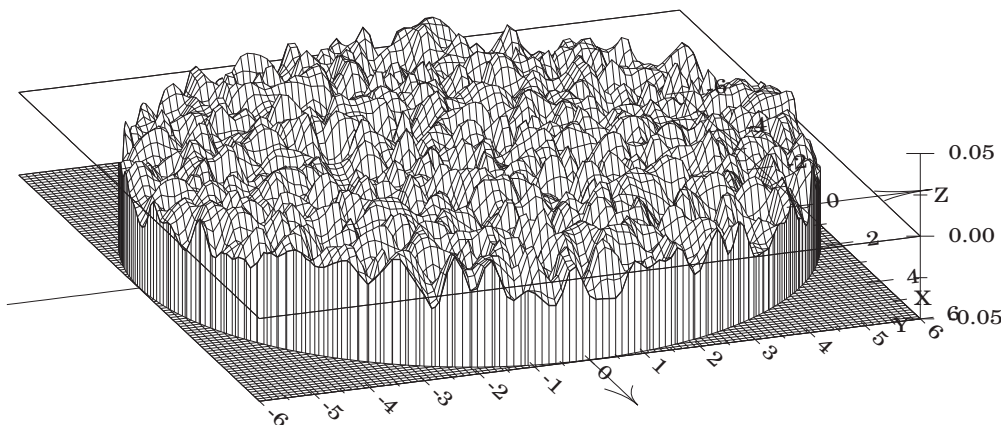


Figure 5-68 Surface shape illustrating the panel manufacturing errors

The following Figures 5-69 to 5-76 show contour plots and pattern cuts for the two types of panel errors separately: the manufacturing errors affecting the shape of the panels and the alignment errors affecting the orientation of the panels. The pattern cuts show the nominal pattern without panel errors in black, the pattern with errors in red and the difference field in green.

The reduction in gain at 243 GHz due to the panel errors is 0.02 dB and 0.00 dB for manufacturing and alignment errors, respectively. The corresponding numbers at 720 GHz are 0.17 and 0.02 dB.

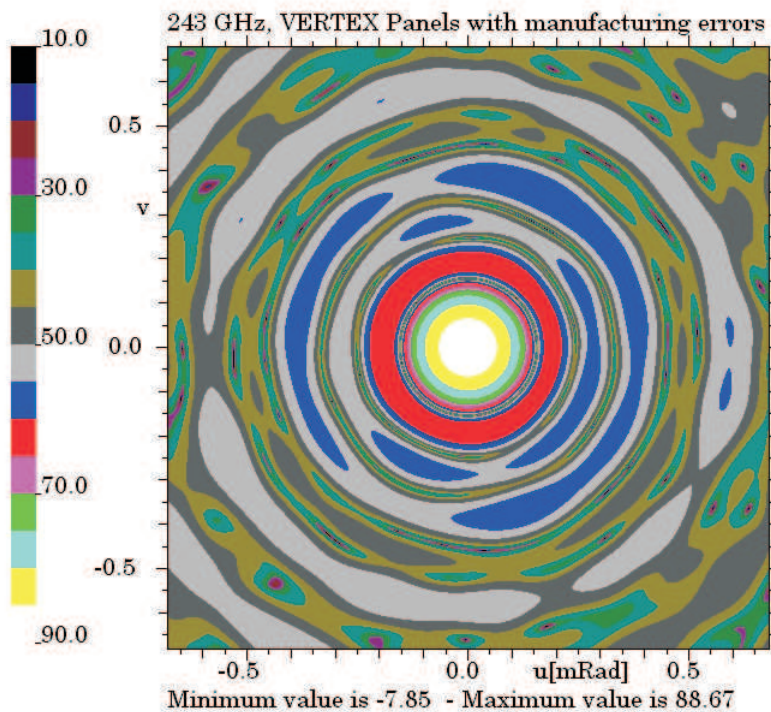


Figure 5-69 Contour plot of the beam at 243 GHz for the Vertex antenna with panel manufacturing errors

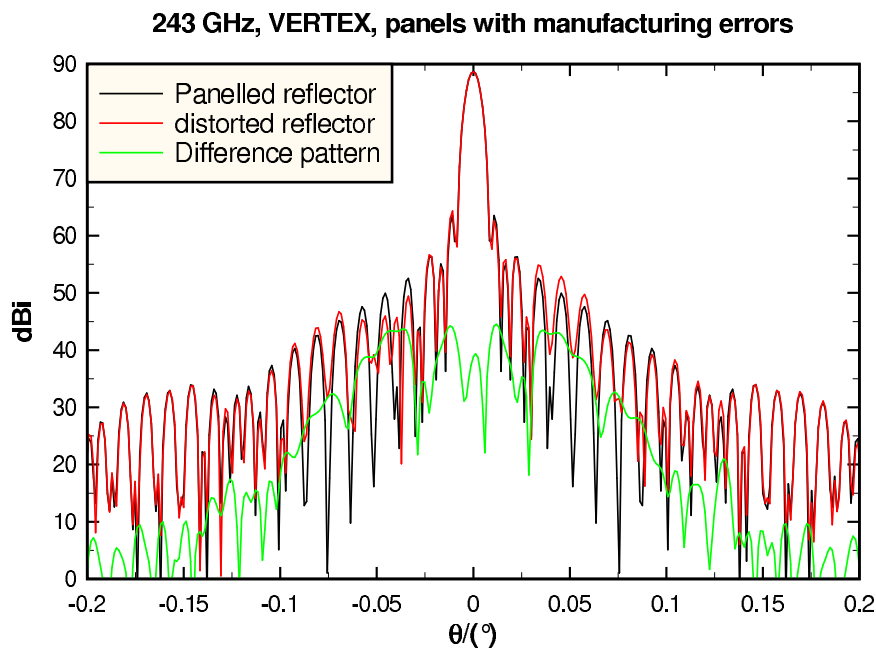


Figure 5-70 Pattern cuts at 243 GHz for the Vertex antenna with panel manufacturing errors

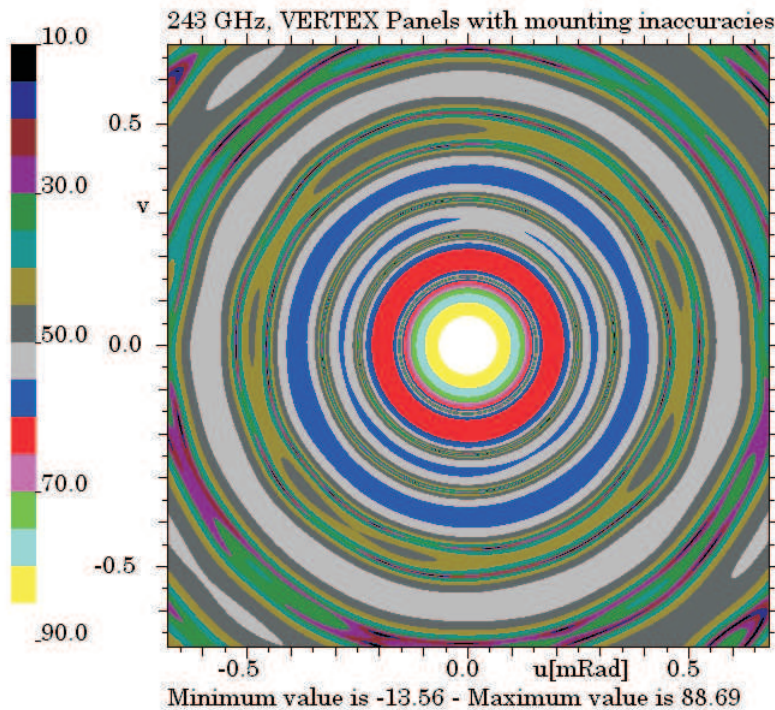


Figure 5-71 Contour plot of the beam at 243 GHz for the Vertex antenna with panel alignment errors

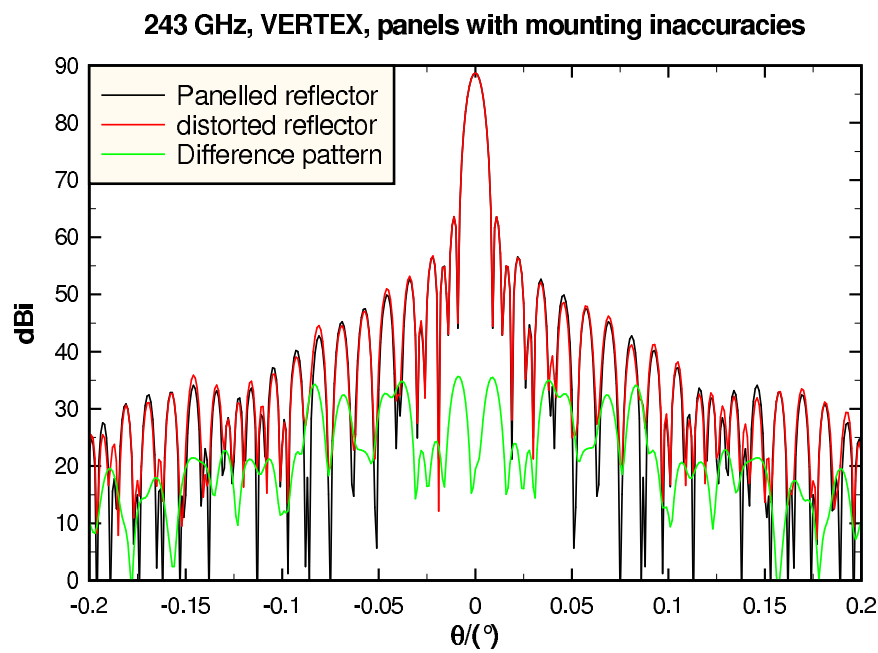


Figure 5-72 Pattern cuts at 243 GHz for the Vertex antenna with panel alignment errors

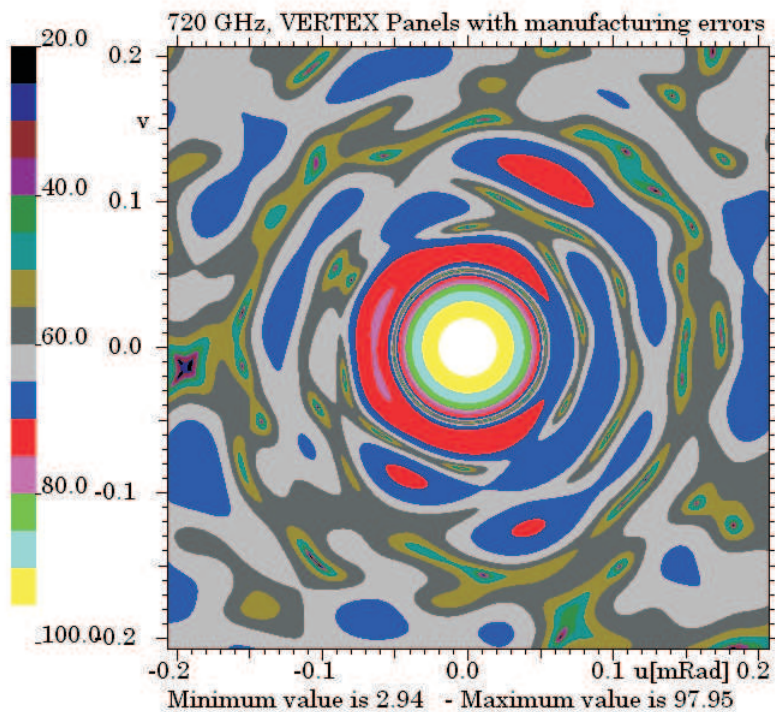


Figure 5-73 Contour plot of the beam at 720 GHz for the Vertex antenna with panel manufacturing errors

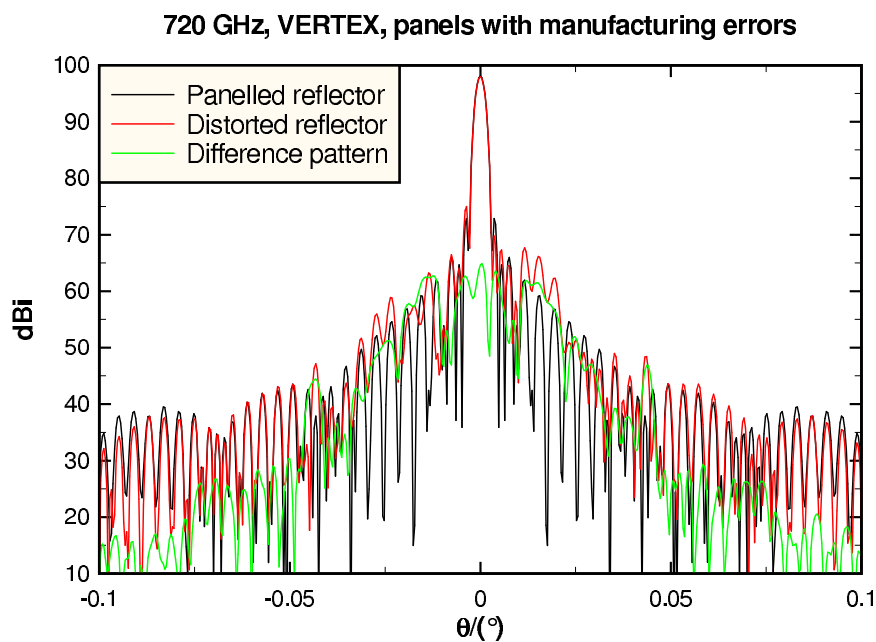


Figure 5-74 Pattern cuts at 720 GHz for the Vertex antenna with panel manufacturing errors

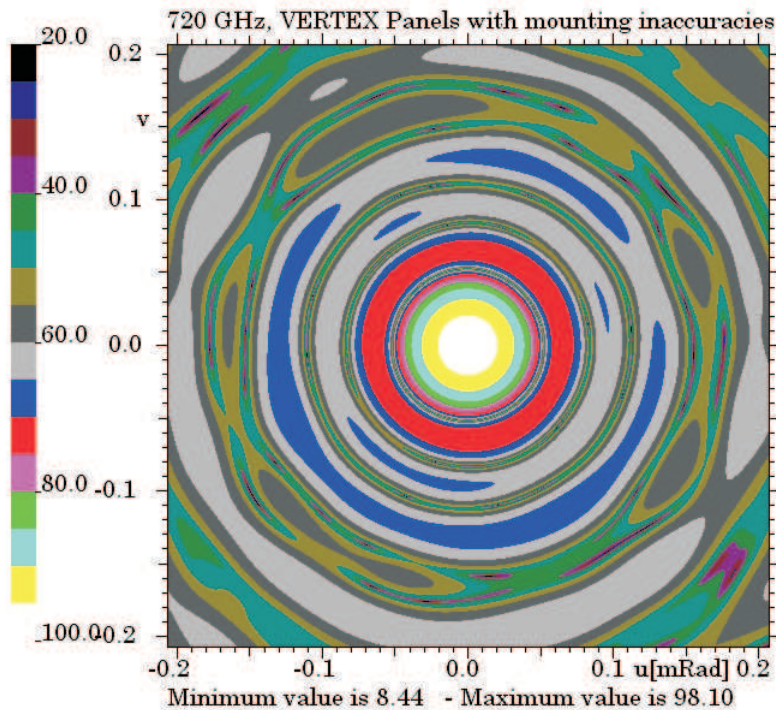


Figure 5-75 Contour plot of the beam at 720 GHz for the Vertex antenna with panel alignment errors

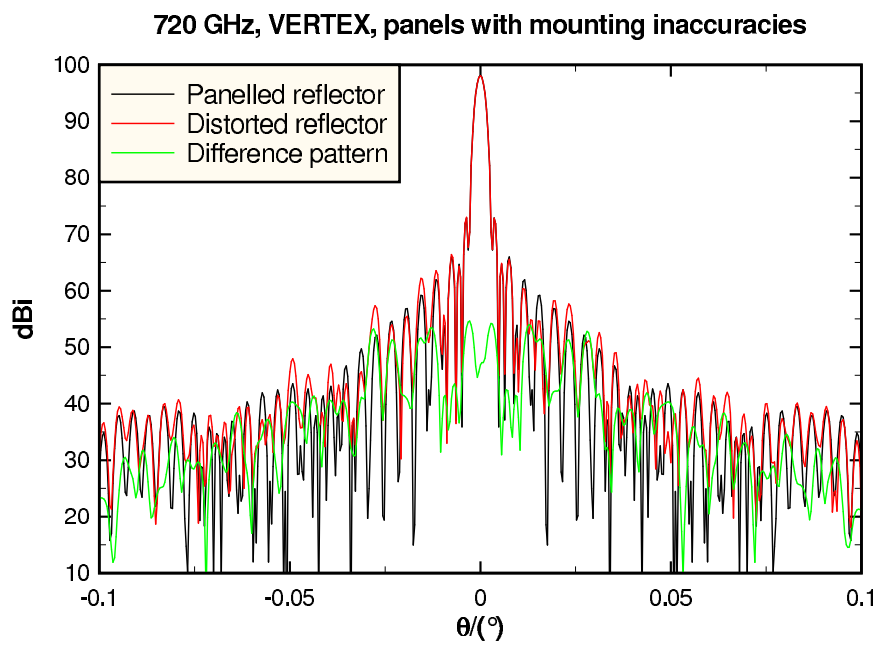


Figure 5-76 Pattern cuts at 720 GHz for the Vertex antenna with panel alignment errors

References

- [1] R. Hills, "RF Membrane", July 2005.
17
- [2] A. M. Baryshev, M. Candotti and N. A. Trappe,
"Cross-polarization characterization of GORE-TEX slabs at
band 9 frequencies", Tech. Rep. ALMA MEMO 551,
NOVA/NUIM, 2006.
17
- [3] D. Koller, G. A. Ediss and A. R. Kerr, "Dielectric Constant of
Goretex RA7956/7957 Radome Material in the Frequency
Range 1 MHz - 2 THz", Tech. Rep. ALMA MEMO 309, NRAO,
2000.
17
- [4] M. Sugimoto, Y. Sekimoto, K. Tatematsu, T. Kamba, H. Toba,
S. Yokogawa, T. Okuda, K. Kohno, T. Noguchi, N. Yamaguchi,
R. Kandori and K. Muraoka, "Cartridge-Type 800 GHz
Receiver for the Atacama Submillimeter Telescope
Experiment (ASTE)", Publications of the Astronomical
Society of Japan, vol. 56, no. 6, pp. 1115–1126, 2004.
17
- [5] J. W. Lamb, "Optimized Optical Layout for MMA 12-m
Antennas", Memo 246, ESO, January 1999, NRAO MMA
MEMO SERIES.
35
- [6] R. A. Ross and M. A. K. Hamid, "Scattering by a wedge with
rounded edge", IEEE Trans. Antennas Propagat., vol. AP-19,
pp. 507–516, July 1971.
44, 47, 49, 51, 53
- [7] M. Carter, "ALMA Front-end Optics Design Report", Tech.
Rep. FEND-40.02.00.00-035-B-REP Draft, ALMA,
2006-12-12.
54, 58, 62, 63, 64, 66, 72, 73, 75, 77, 81, 82, 86, 87, 90, 93, 95,
96, 97, 98, 105, 108
- [8] M. Carter, R. Nesti, "ALMA Front-end Optics Design Report,
Appendix 1", Tech. Rep. FEND-40.02.00.00-035-B-REP,
IRAM, 2007-02-14, First Version.
54
- [9] M. Carter, R. Nesti, "ALMA Front-end Optics Design Report,
Appendix 2", Tech. Rep. FEND-40.02.00.00-035-B-REP,
IRAM, 2007-02-14, First Version.
54, 56

- [10] M. Carter, F. Coq, A. L. Fontana, F. Tercero, J. A. Lopez Fernandez, C. Y. Tham, D. Erickson, “ALMA Front-end Optics Design Report, Appendix 3”, Tech. Rep. FEND-40.02.00.00-035-B-REP, IRAM, 2006-11-22, Draft. 54, 59, 60, 61, 63, 64, 68, 69, 70, 72
- [11] S. Asayama, H. Iwashita, M. Sugimoto, “ALMA Front-end Optics Design Report, Appendix 4”, Tech. Rep. FEND-40.02.00.00-035-B-REP, NAOJ, 2007-01-29, Draft. 54, 74, 75, 76, 77
- [12] M. Carter, F. Coq, B. Lazareff, “ALMA Front-end Optics Design Report, Appendix 6”, Tech. Rep. FEND-40.02.00.00-035-B-REP, IRAM, 2007-01-22, First Version. 54, 81, 83, 85, 91, 93
- [13] M. Carter, P. Serre, F. Coq, S. Mahieu, A. L. Fontana, D. Maier, “ALMA Front-end Optics Design Report, Appendix 7”, Tech. Rep. FEND-40.02.00.00-035-B-REP, IRAM, 2006-12-12, First Version. 54, 94, 95, 96, 102
- [14] M. Candotti, “ALMA Front-end Optics Design Report, Appendix 9”, Tech. Rep. FEND-40.02.00.00-035-B-REP, NOVA/SRON/NUIM, 2006-12-01, First Version. 54, 97, 105, 106, 107, 108, 113
- [15] R. Johnson and H. Jasik, “Antenna engineering handbook”, McGraw-Hill, 1984. 61
- [16] A.L. Fontana, M. Carter, B. Lazareff, F. Coq, “ALMA Band 3 Horn: Final Report”, Tech. rep., IRAM, 2004-10. 62, 63
- [17] ESO, “Table 2: ALMA Cartridge, WVR, Windows and IR-filters mechanical information”, Tech. Rep. Table2 Window and IR FILTERS.pdf, ESO, 2007. 64, 75, 87
- [18] J. Lesurf, “Millimetre-wave optics, devices and systems”, Adam Hilger, 1990. 83
- [19] M. Candotti, M. Matsunaga, Y. Uzawa, “ALMA Front-end Optics Design Report, Appendix 10”, Tech. Rep. FEND-40.02.00.00-035-B-REP, NAOJ, 2007-07-04, First Version. 114
- [20] M. Carter, A. L. Fontana, F. Mattiocco, B. Lazareff, K. Hara, M. Sugimoto, “ALMA Front-end Optics Design Report, Appendix 11”, Tech. Rep. FEND-40.02.00.00-035-B-REP, IRAM/NAOJ, 2006-10-24, First Version. 116